Inviscid and Viscous CFD Analysis of Booster Separation for the Space Launch System Vehicle

Derek J. Dalle[*],

Science and Technology Corp., Moffett Field, CA 94035

Stuart E. Rogers[†], William M. Chan[‡],

NASA Ames Research Center, Moffett Field, CA 94035

Henry C. Lee[§]

Science and Technology Corp., Moffett Field, CA 94035

This paper presents details of Computational Fluid Dynamic (CFD) simulations of the Space Launch System during solid-rocket booster separation using the Cart3D inviscid and Overflow viscous CFD codes. The discussion addresses the use of multiple data sources of computational aerodynamics, experimental aerodynamics, and trajectory simulations for this critical phase of flight. Comparisons are shown between Cart3D simulations and a wind tunnel test performed at NASA Langley Research Center's Unitary Plan Wind Tunnel, and further comparisons are shown between Cart3D and viscous Overflow solutions for the flight vehicle. The Space Launch System (SLS) is a new exploration-class launch vehicle currently in development that includes two Solid Rocket Boosters (SRBs) modified from Space Shuttle hardware. These SRBs must separate from the SLS core during a phase of flight where aerodynamic loads are nontrivial. The main challenges for creating a separation aerodynamic database are the large number of independent variables (including orientation of the core, relative position and orientation of the boosters, and rocket thrust levels) and the complex flow caused by exhaust plumes of the booster separation motors (BSMs), which are small rockets designed to push the boosters away from the core by firing partially in the direction opposite to the motion of the vehicle.

Nomenclature

C_A	=	CA, Axial force coefficient, body axis	t	=	Time since separation
C_{LL}	=	CLL, Rolling moment coefficient	w	=	Linear combination weight for output function
C_{LM}	=	CLM, Pitching moment coefficient	$\mathbf{x}$	=	Position vector
C_{LN}	=	CLN, Yawing moment coefficient	α	=	*alpha*, Angle of attack of the core
C_N	=	CN, Normal force coefficient, body axis	β	=	*beta*, Angle of sideslip of the core
C_T	=	Thrust coefficient	$\Delta\phi$	=	*dphi*, Roll angle of SRB relative to core
C_Y	=	CY, Side force coefficient, body axis	$\Delta\psi$	=	*dpsi*, Yaw angle of SRB relative to core
L_1	=	Residual based on sum of absolute values	$\Delta\theta$	=	*dtheta*, Pitch angle of SRB relative to core
M	=	Freestream Mach number	Δx	=	*dx*, Axial displacement of booster nose
p	=	Static pressure	Δy	=	*dy*, Lateral displacement of booster nose
q	=	Freestream dynamic pressure	Δz	=	*dz*, Vertical displacement of booster nose
r	=	Radius from center of core	σ	=	Standard deviation

[*]Research Scientist/Eng., Computational Aerosciences Branch, Member AIAA, `derek.j.dalle@nasa.gov`

[†]Aerospace Eng., Computational Aerosciences Branch, Associate Fellow AIAA, `stuart.e.rogers@nasa.gov`

[‡]Computer Scientist, Computational Aerosciences Branch, Senior Member AIAA, `william.m.chan@nasa.gov`

[§]Research Scientist/Eng., Computational Aerosciences Branch, Member AIAA, `henry.c.lee@nasa.gov`

Abbreviations

BSM   =   Booster Separation Motor   RSRB   =   Right Solid Rocket Booster
CFD   =   Computational Fluid Dynamics   SLS   =   Space Launch System
CSE   =   Core Stage Engine   SRB   =   Solid Rocket Booster
LSRB =   Left Solid Rocket Booster   UPWT   =   Unitary Plan Wind Tunnel (NASA Langley)

I.   Introduction

The Space Launch System (SLS) is a new exploration-class launch vehicle currently in development by NASA and a team of contractors and will be the first exploration-class launch vehicle since Saturn V. To achieve its mission, SLS will use Solid Rocket Boosters (SRBs) that are slightly modified hardware from the Space Shuttle Launch Vehicle. These SRBs expend their fuel long before the SLS core first stage, and thus there is a separation event that must occur during a phase of flight where aerodynamic loads are nontrivial. A drawing of SLS with the two SRBs attached on the left and right sides is shown in Fig. 1.

Since gravity is not acting in a way that pulls the expended boosters away from the core, and aerodynamic loads also do not act in a way to substantially encourage separation, small rockets called Booster Separation Motors (BSMs) are used to actively push the boosters away from the core. There are 16 of these BSMs—four forward BSMs and four aft BSMs on each booster. The forward BSMs fire in a partially forward (upstream-facing) direction, which results in complex plumes and interactions of those plumes with the high-speed freestream flow. In addition, the low dynamic pressure during the separation event com-
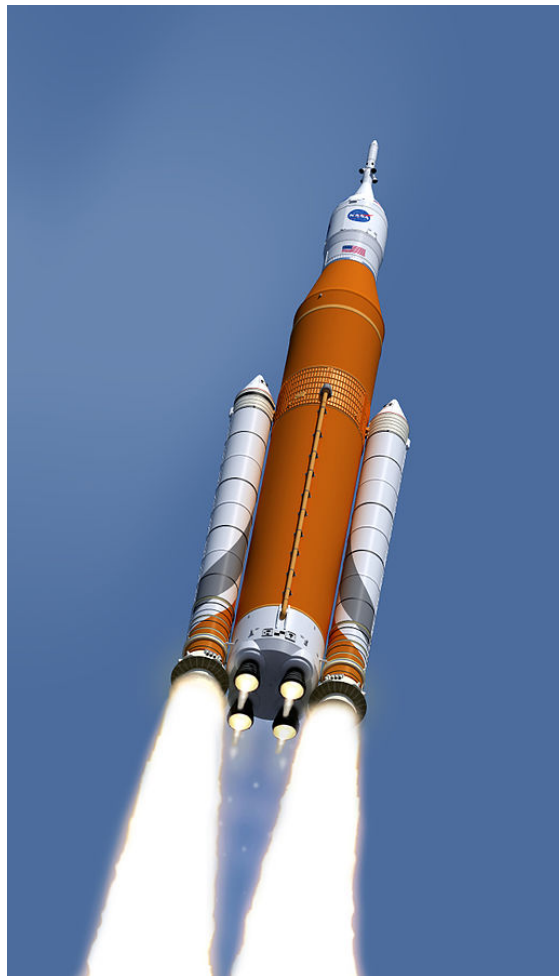

Figure 1. Artist rendition of the SLS Block 1 configuration

American Institute of Aeronautics and Astronautics

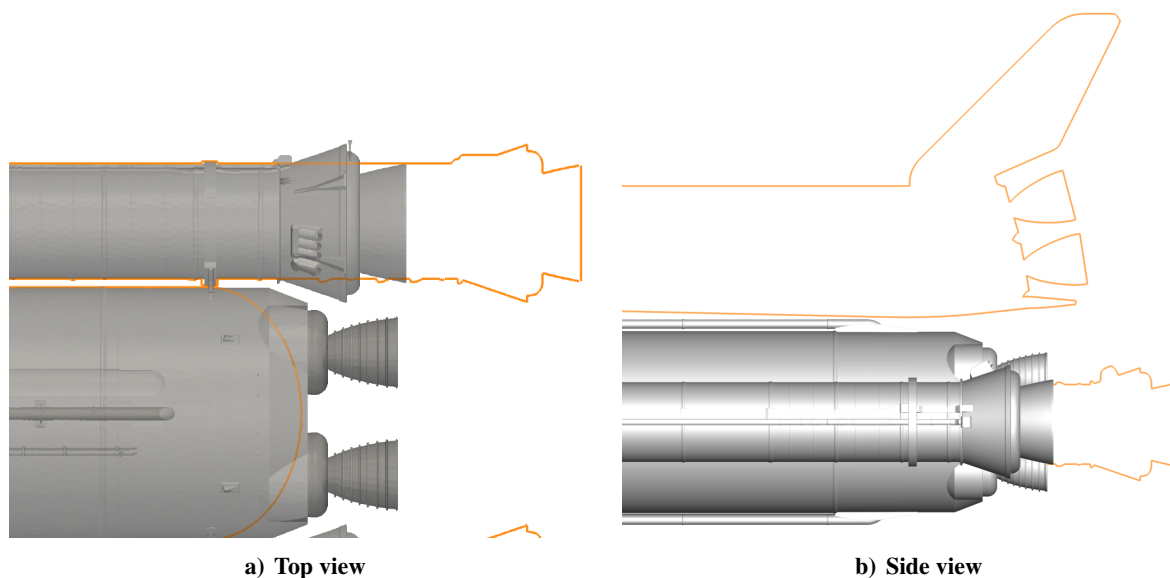**a) Top view**　　　　　　　　　　　　　　　　　**b) Side view**

Figure 2. Comparison of attached booster positions for SLS (grey) and Space Shuttle Launch Vehicle (orange outline)

bined with the relatively high-thrust separation motors means that the plume affects a very large volume of flow—on the scale of the SLS vehicle itself.

The SRBs are similar to Space Shuttle hardware, which have a rich history of successful flights. However, separating from the SLS core is more challenging than separating from the Space Shuttle External Tank Figure 2 shows an overlay of the two vehicles. The reason for this is simple: whereas the External Tank essentially ended at the point where the SRBs were attached, SLS has a substantial amount of hardware, including its main engines, directly aft of the SRB attachment point. As a result of the change in configuration with no corresponding design change in the separation mechanism, clearances between the aft portion of the SRB and the aft portion of the SLS core stage can be small. Furthermore, the closer proximity of the booster and core stage engines results in more plume interactions that make the flow more challenging to simulate. To have sufficient confidence that no recontact will occur during flight, achieving a small aerodynamic uncertainty is essential. Furthermore, determining a defensible uncertainty becomes an important part of the aerodynamic database.

Another aspect that makes CFD for this portion of flight challenging is the vast number of orientations and conditions that must be simulated. The separation occurs within a finite window of time within a range of temperatures and altitudes, and the rest of the vehicle has its own uncertainties during ascent that make the separation environment even less concrete. Assuming symmetry between the left and right boosters, there are six degrees of freedom for the position and orientation of the boosters, two degrees of freedom for the orientation of the core, two more degrees of freedom for Mach number and dynamic pressure, and a range of possible thrust conditions. After further simplifications, the database produced for this effort was 8-dimensional and required more than 20,000 CFD simulations. The run matrix and the decisions that went into it are discussed in Sec. II.

Due to the immense size of this run matrix, the decision was made to utilize Cart3D both for its speed and ease of setup. Cart3D [1, 2] is a solver developed at NASA Ames with exactly these capabilities and uses an cut-cell Cartesian grid approach that makes volume mesh generation automatic. The solver also has a history of use with powered rocket boundary conditions, including nozzles that are small relative to the scale of the vehicle, from its use in support of the Orion program [3, 4]. The run methodology developed for Cart3D in this task is highlighted in Sec. III. This work builds on previous efforts for the similar Ares-V vehicle [5], design and analysis cycle 2 for SLS [6], and critical design review for SLS [7]. Some lessons for the less similar Ares-I configuration [8, 9] were also applied to the present effort.

American Institute of Aeronautics and Astronautics

Compared to the intermediate database discussed in [7], this work addresses improved run strategies for Cart3D and Overflow, completion of the database to cover the entire separation maneuver, concentration of CFD simulations around the nominal trajectory, inclusion of a separate database to model the case that a core engine fails, and delivery or more detailed information for uncertainty quantification.

The inviscid assumption is tentatively acceptable due to the high supersonic Mach number (greater than 4.0) at separation and low dynamic pressure. However, complex flow and large boundary layers imply that viscous effects merit consideration, and full Reynolds-Averaged Navier-Stokes Overflow [10] simulations have been used to evaluate this assumption and provide an increment to the flight database uncertainty quantification that accounts for viscous effects. Overflow is a solver developed at both NASA Langley and NASA Ames using overset structured grid technology. Section IV covers the run strategy used for Overflow in this work including a discussion of mesh adaption applied to this complex configuration.

In order to increase confidence in the booster separation database, a wind tunnel test was conducted at NASA Langley Research Center's Unitary Plan Wind Tunnel [11]. Different from many high-profile aerodynamic databases, resources were not available to conduct a wind tunnel test that could be used to construct a flight database. Instead, the Cart3D results discussed in this paper are the underlying data source for the booster separation aerodynamic database while the Overflow and wind tunnel test results contribute to the uncertainty analysis. The results presented in Sec. V focus on direct comparisons between Cart3D and the wind tunnel test and between Cart3D and Overflow results. In combination, these results demonstrate the capability to construct an extremely large aerodynamic database with complex flowfields and a detailed vehicle geometry. Even including the conservatism necessarily attached to human-rated rockets, the results demonstrate high enough quality throughout the database that uncertainty bounds need not be excessively large.

II.   Independent Variables and Run Matrix

The aerodynamic database is a function of eight variables, which are described in Table 1. A text-only name for each variable is provided to make references to them a little simpler; a more traditional mathematical symbol is also provided in Table 1. These variables can be divided into four groups: booster translations, *dx*, *dy*, *dz*; booster rotations, *dpsi* and *dtheta*; core orientations, *alpha* and *beta*; and booster separation motor thrust, *CTBSM*. Furthermore, most of these are grouped into three pairs: *dy* and *dz*, *dpsi* and *dtheta*, and *alpha* and *beta*.

Table 1. Input variables for separation aerodynamic database

Variable	Symbol	Description
dx	Δx	Booster axial translation [ft]
dy	Δy	Booster lateral translation, away from core [ft]
dz	Δz	Booster translation in +z-direction [ft]
dpsi	$\Delta \psi$	Booster yaw angle relative to core body axes [deg]
dtheta	$\Delta \theta$	Booster pitch angle relative to core body axes [deg]
alpha	α	Angle of attack of the core [deg]
beta	β	Angle of sideslip of the core [deg]
CTBSM	$C_{T,BSM}$	Booster separation motor thrust coefficient

Axial booster translation, *dx*, is a special variable that is used to schedule each of the other variables. For example, let dx_i be a particular value of *dx*, such as 8 ft. The aerodynamic database includes CFD solutions at three values of *dy*: $dy_{i,\min}$, $dy_{i,\text{nom}}$, and $dy_{i,\max}$. These minimum, nominal, and maximum values come from a full six-degree-of-freedom simulation by the guidance, navigation, & control group using a lower-fidelity aerodynamic database with large uncertainties. In addition, these minimum, nominal, and maximum translations have different values at each *dx*. The same description also holds for the remaining six variables, although some values of *CTBSM* are omitted at higher *dx* when the thrust is very low.
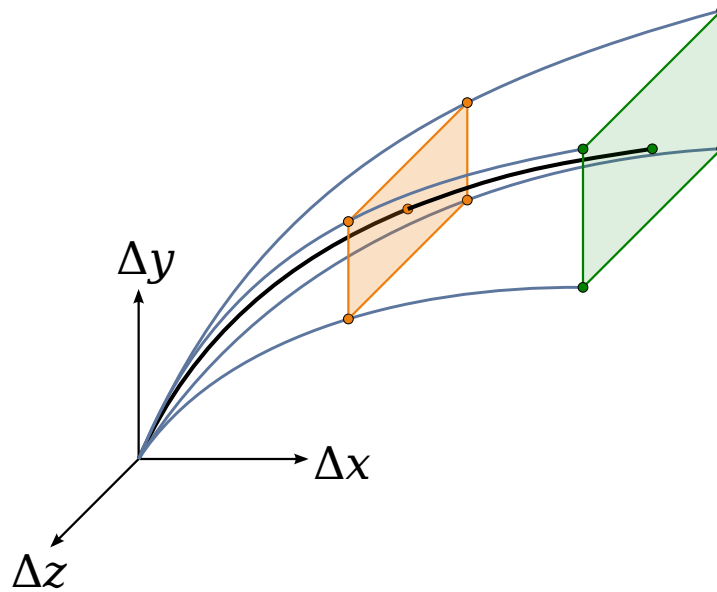
Figure 3. Sketch of run matrix concept; circles represent points and translucent shapes are cross sections at one *dx* value

To prevent requiring roughly 3^8=6561 CFD simulations at each dx_i to cover three values of eight variables, variables are grouped into three pairs. For each pair, the only simulations included are the nominal-nominal pair plus each of the four min-max, min-min, etc. corners. The minimum, nominal, and maximum values for each variable change as a function of dx, resulting in a curved pyramid shape for the run matrix. An example visualization of this approach is shown in Fig. 3. The example pair used in the figure is the booster translation pair of *dy* and *dz*. Two values of *dx*—one lower (orange rectangle) and one higher (green rectangle)—are shown. The filled circles (five in each of the two *dx* slices shown) are the points included in the run matrix. The nominal reference trajectory is shown as the thick black curve through the middle of the slices. The blue curves represent the corner trajectories that follow either the minimum or maximum value of both *dy* and *dz*. Using this approach reduces the number of points at each slice from 9 (if each combination of minimum, nominal, or maximum were included) to 5, which seems like a small reduction. However, this process is repeated for the other pairs of *dpsi-dtheta* and *alpha-beta*. Combining these 5/9 reductions for three pairs results in an 83% reduction in the number of simulations.

Finally, there are several more input variables that play a role but do not increase the dimensionality of the database. These include variables such as Mach number and dynamic pressure that change during the booster separation but do not vary enough or have a significant effect on overall aerodynamics. Another important value is the thrust from the core's main engines, which is programmed to increase in time from the moment the boosters separate. Since there is very little expected dispersion of the core-main engine thrust from the programmed values, nominal values are used in the simulations and there is no need to add more simulations to the run matrix. On the other hand, the SRB thrust has a wider dispersion during the separation event, but has only a small effect on aerodynamics. The full list of such variables is described in Table 2.

This entire run matrix was simulated three times; once for the nominal case where all core engines operate properly and two more times for the situation that one of the core engines fails. There are four engines, and symmetry was applied to eliminate the need to analyze a failure of either left engine. Analysis of the failure of a single booster separation motor (BSM) was also requested, but an initial investigation showed that BSM failure could be covered by the nominal database. Thus there were three run matrices: one for the nominal ascent, one for a failure of the top right core engine, and one for a failure of the bottom

American Institute of Aeronautics and Astronautics

Table 2. Variables scheduled as a function of *dx*

Variable	Symbol	Description
t	t	Time since separation [s]
dphi	$\Delta\phi$	Booster roll angle relative to core body axes [deg]
mach	M	Core Mach number
q	q	Core dynamic pressure [psf]
CTCSE	$C_{T,CSE}$	Core stage engine thrust coefficient
CTSRB	$C_{T,SRB}$	Solid rocket booster thrust coefficient

right core engine. Engine failures can occur at any time, and the vehicle makes adjustments to the trajectory to compensate for the failure. As a result of these two factors, the run matrix for core engine failure scenarios is different from and has a much wider dispersion than the nominal run matrix.

III. Cart3D Run Strategy

The primary advantages of using Cart3D for this type of database are its speed, efficient handling of geometric complexity, and adaptive meshing capability. Even so, this particular configuration has enough complexity that special care should be taken to develop a run strategy that utilizes these Cart3D advantages efficiently. The approach used here takes advantage of Cart3D's output-based mesh adaptation. Starting from a relatively coarse initial mesh with about 150,000 volume cells, five adaptation cycles are used, which grows the mesh size to about 16 million cells.

A. Cart3D Volume Meshing

The output function used to drive this mesh adaptation is

$$J = C_{Y,LSRB} + C_{Y,RSRB} + 0.5C_{N,LSRB} + 0.5C_{N,RSRB} + 0.5C_{A,LSRB} + 0.5C_{A,RSRB}$$

$$+ 0.5C_{A,CORE} + C_{Y,CORE} + 0.5C_{N,CORE} + \sum_{i=1}^{13} w_i \frac{p(\mathbf{x}_i) - p_\infty}{p_\infty} \tag{1}$$

In output-based mesh adaptation, an adjoint solution is computed after the flow solution using the same (or similar) mesh. The adjoint measures how sensitive a user-defined output function, like that defined in Eq. (1), is to residuals in each cell. That information is used to determine how much a refinement of each cell (i.e. splitting one volume cell into eight smaller ones with half the side length of the original cell), which leads to a ranking of which volume cells would be best to refine. The output function used here includes all three force coefficients (C_A, C_Y, and C_N) on all three bodies (LSRB, RSRB, and CORE) with roughly equal weights. A slight emphasis is placed on the lateral forces, which have the biggest impact on the success or failure of the separation maneuver. This output function also utilizes 13 point sensors at selected locations toward the front of the vehicle. Each point sensor measures static pressure at a point $\mathbf{x}_i$ minus freestream pressure, nondimensionalized by freestream pressure [12]. These point sensors all have weights between 0.001 and 0.005 and focus on points in the volume solution that affect the integrated forces and moments but are difficult to resolve on the early coarser meshes. The details are presented in Table 3 where clocking angle θ gives angular location via $z=r\cos\theta$ and $y= -r\sin\theta$. The origin is 1009.1 inches in front of the nose of the core, which was chosen to represent a point in the Vehicle Assembly Building.

Fortunately, the results are not sensitive to the details of the locations of these point sensors, but including a few of them had a beneficial impact on the consistency of the final flow solutions. In total, the sum of the pressure sensors is about 10% to 30% of the total value of the combined functional. The decision to use point sensors to augment the output function was based on an extensive input sensitivity study, which showed that they added robustness to the system.

American Institute of Aeronautics and Astronautics

Table 3. Output function point sensor locations and weights

i	Axial location (x_i)	Radius (r_i)	Clocking angle (θ_i)	Weight (w_i)
1	2000 in	200 in	0°	0.005
2	2000 in	300 in	90°	0.005
3	2000 in	300 in	270°	0.005
4	2400 in	200 in	180°	0.002
5	2600 in	800 in	0°	0.002
6	3000 in	300 in	30°	0.001
7	2000 in	300 in	60°	0.001
8	2000 in	300 in	120°	0.001
9	3000 in	300 in	150°	0.001
10	3000 in	300 in	210°	0.001
11	2000 in	300 in	240°	0.001
12	2000 in	300 in	300°	0.001
13	3000 in	300 in	330°	0.001

In addition to geometric complexity, the SLS booster separation problem also was subject to a wide range of scales. The BSM boundary condition planes are just a few inches in diameter while the full vehicle is well over 300 ft in length. The BSMs are extremely important for the overall aerodynamics of the configuration, and so meeting the challenge to resolve them on the initial mesh is critically important. Fortunately, Cart3D has two features that enable tailored initial meshes appropriate for this task. First, the Cart3D volume meshing program called *cubes* creates a mesh that has finer cells closer to the surface of the vehicle. With the settings used here, this first pass at the volume mesh has its finest cells with sides of about 100 in. Next, inputs are prescribed using Cart3D's *XLev* setting to request five additional levels of refinement for any volume cell containing a part of any BSM boundary condition plane or nozzle interior surface, which is fine enough to put a few cells inside each BSM. Finally, several of Cart3D's *BBox* specifications are defined to create a finer mesh in certain volumes. These boxes are defined as a minimum and maximum coordinate for *x*, *y*, and *z* along with a minimum number of refinements for cells within that box. For the SLS booster separation configuration, two regions of the volume were refined in this manner: the core engine plumes and the forward region of the core where the forward BSM exhaust plumes have complex behavior. These forward volumes benefit from higher resolution on the initial meshes so that the interaction between upstream vorticity (due to both curved shocks and losses near the abort motor nozzles) and BSM exhaust can be captured earlier in the mesh adaptation sequence. The details of these initial mesh considerations, along with a discussion of the consequences of missing this effect, can be found in [7].

At each level of mesh adaptation, the flow is run for 500 iterations, which results in 3000 total iterations (`adapt00` through `adapt05`). Each adaptation cycle increases the number of volume cells in the mesh by a user-specified ratio, and the mesh growth ratios used for this work were 1.5, 2.0, 3.0, 4.0, and 3.5. For simulations in which the BSMs are on, which tend to be unsteady, an additional 3000 or more steady-state iterations are completed on the final mesh in order to calculate mean values for each of the force and moment coefficients.

B.   Steady-State and Time-Accurate Comparisons

Solutions for the nominal separation trajectory using time-accurate inputs to Cart3D were simulated in order to quantify the differences in forces and moments between steady-state and time-accurate solutions. The time-accurate solutions used ten subiterations at each time step and a nondimensional time step of 0.1, meaning that a particle traveling the freestream speed of sound moves 0.1 grid units (in this case, inches) each time step. The results, shown in Fig. 4, show consistent results between the two solution approaches,
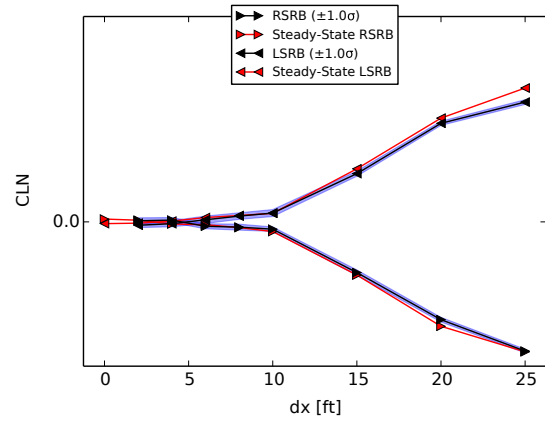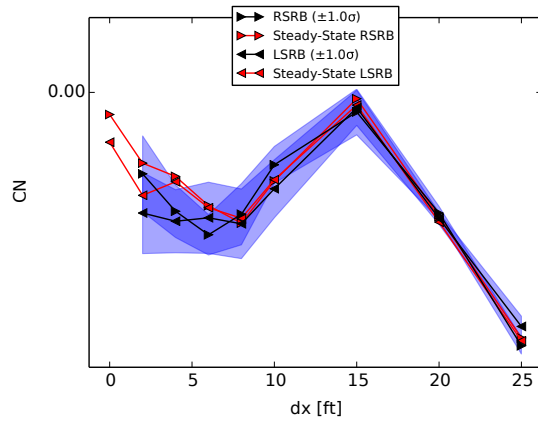
American Institute of Aeronautics and Astronautics
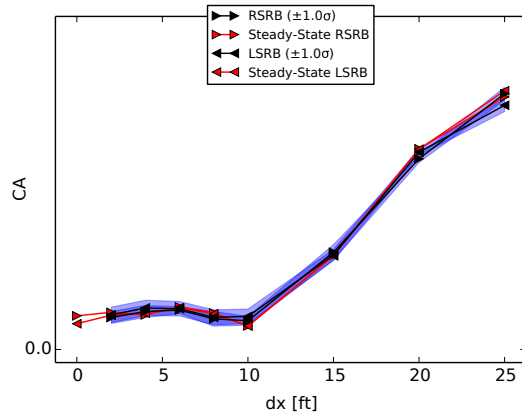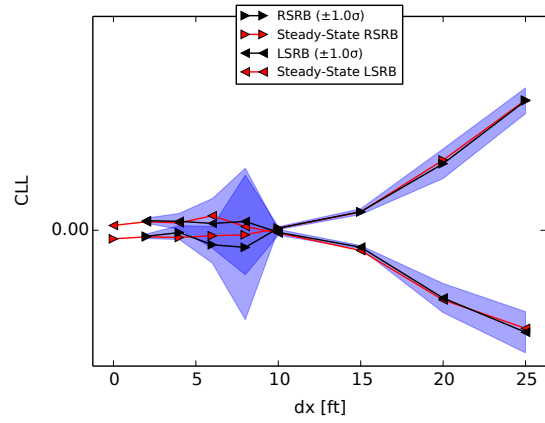
a) Axial force, *CA*

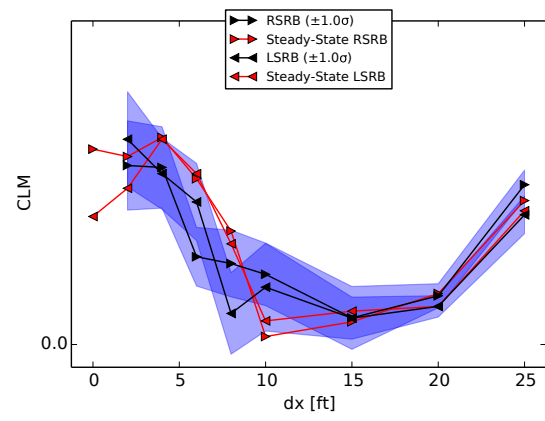**b) Rolling moment, *CLL***
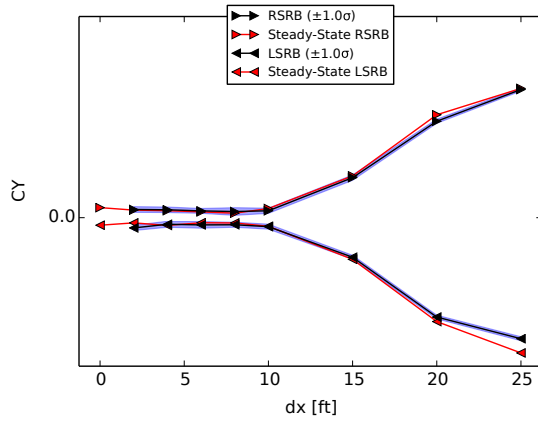
c) Axial force, *CA*

d) Yawing moment, *CLN*

e) Axial force, *CA*

f) Pitching moment, *CLM*

Figure 4. Comparison of time-accurate (black) and steady-state (red) Cart3D results and moments for nominal BSM-on trajectory. Standard deviation of time-accurate history shown in blue.
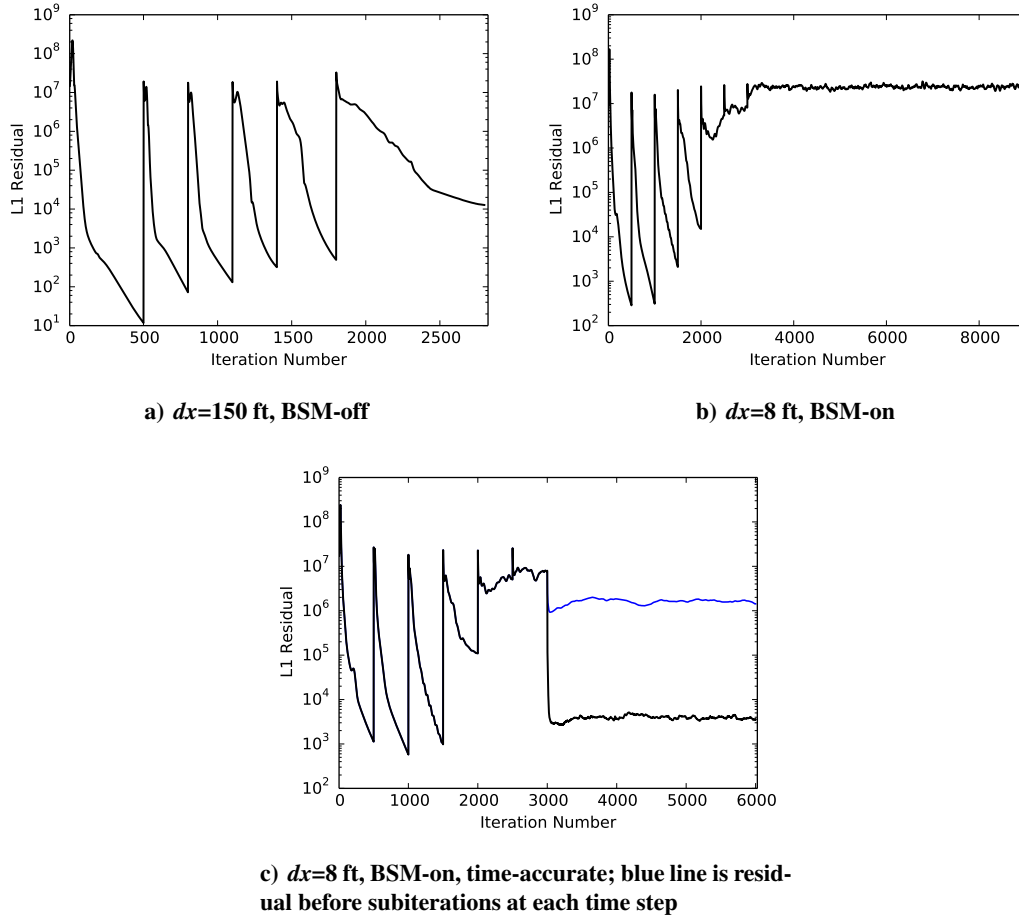
American Institute of Aeronautics and Astronautics

a) *dx*=150 ft, BSM-off

b) *dx*=8 ft, BSM-on

c) *dx*=8 ft, BSM-on, time-accurate; blue line is residual before subiterations at each time step

Figure 5. History of Cart3D L_1 density residuals for selected cases

and thus steady-state inputs were used to construct the database. This constitutes significant savings since the steady-state solutions required about seven times more CPU-hours.

Figure 5 shows residual histories for the three main categories of Cart3D solutions relevant to this work. When the BSMs are not firing, convergence is consistently good, which is shown by example in Fig. 5a. However, when the BSMs are firing at full strength in the first second or so of the separation, convergence on the final mesh is usually poor or nonexistent, as shown in Fig. 5b. This result, while discomfiting, is typical when using a steady-state solution method for an unsteady problem. When using time-accurate inputs for the same conditions as Fig. 5b, convergence can be obtained, as shown in Fig. 5c. The blue line between iteration 3000 and iteration 6000 shows the residual before any subiterations at each time step, and the black curve over this same period shows the residual after subiterations; the difference between these two shows the amount of convergence obtained at each time step. The combination of time-accurate convergence as shown in Fig. 5c and good comparison between time-accurate and steady-state results shown in Fig. 4 serves as the justification to use steady-state solutions for the bulk of the database. However, this weak convergence is taken into consideration when developing an uncertainty model at a later step.

IV. Overflow Run Strategy

The Overflow solutions were computed using the standard release version 2.2k of the Overflow code, using the Message-Passing Interface (MPI) parallel version. The computations were performed on the SGI Altix-Ice system known as *Pleiades* at the NASA Advance Supercomputing (NAS) center. All of the runs used 25 Haswell nodes with 24 cores each, for a total of 600 cores per run.

a) **BSM on, dx=10 feet** b) **BSM off, dx=8 feet**
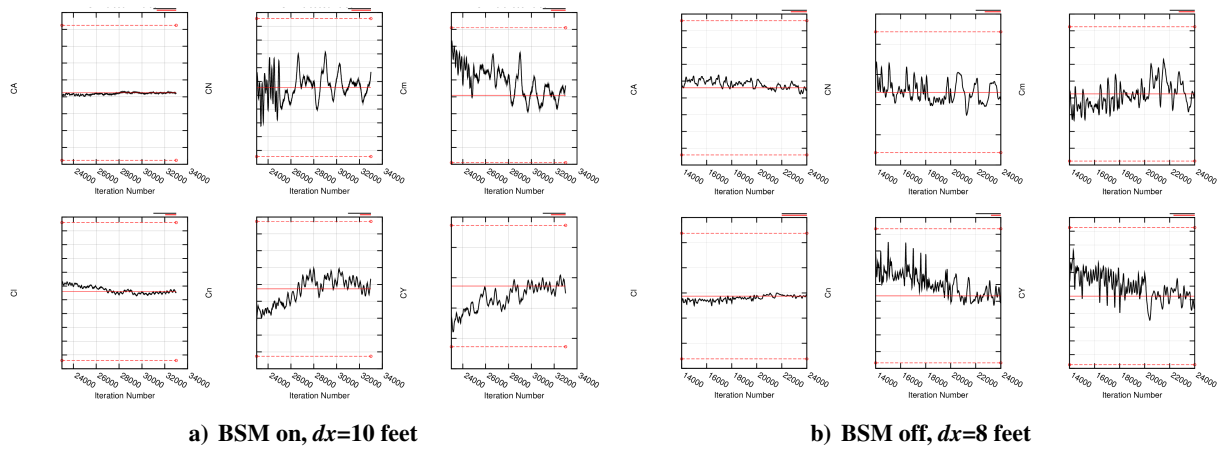
Figure 6. Convergence histories of forces and moments on the right booster for two Overflow simulations.

The third-order HLLC upwind differencing scheme was used in Overflow. The SSOR implicit scheme was used as it was found to retain numerical stability in nozzle flow regions. Local time-stepping with a constant CFL number was used, and all viscous terms, including cross terms, were enabled in the code. A slow start over the first 500 iterations was used for the nozzle inflow boundary conditions.

The overset grid system contained 469 body-fitted zones with over 160 million grid points. Together with the off-body grid adaptation, a total of 250 million grid points were used for each run. The final adapted meshes contained about 5000 to 6000 off-body zones. The grids in the BSM nozzles, the core-stage-engine nozzles, and the booster nozzles all included a short plenum upstream of the nozzle throat. The plenum ended in a planar boundary where uniform nozzle boundary conditions are applied. Boundary-conditions were generated for each nozzle which specified the the desired total pressure and total temperature conditions. These were generated using isentropic relations and the area ratio between the throat area and the boundary-condition surface area to compute the static flow conditions on the nozzle inflow boundary. The specified velocity vector was made normal to the boundary-condition face; care was taken to ensure this was done properly for the booster main nozzles and BSM nozzles to account for the pitch and yaw of the booster. Different gas species were used for each of the three types of nozzles, and Overflow was run using a variable gamma formulation. Calibration cases were run to provide the ratio between the total pressure and the resulting thrust, allowing the proper thrust to be achieved in all subsequent production cases.

The Spalart-Allmaras turbulence model was used and the flow was assumed to be turbulent everywhere. Each simulation was initialized with freestream flow, and started execution using full-multigrid sequencing for 4000 steps. The code continued with steady-state iterations using locally-varying time step sizes until a total of 20,000 iterations were run, then the case was continued with time-accurate integration. This used a dual time step approach with 2 Newton subiterations per time step. They were run until the time-averaged mean of the vehicle forces were converged, and the final solution was extracted from a time average of the last 2000 time steps. A nondimensional time step of 1.0 was used, meaning that a particle moving at the freestream speed of sound moves one inch in each time step. The force and moment histories of multiple components were monitored to determine when a case converged, including the core, and the right and left boosters. A total of 8 million core hours were used to perform the 390 Overflow simulations, with an average time per case of just under 21,000 core hours.

Some example convergence histories of the force and moment coefficients on the right booster are plotted in the following figures. Figure 6a shows the history of the force and moment coefficients for the nominal case with BSMs firing at $dx = 10$ feet. Figure 6b shows the history of the force and moment coefficients for the nominal case with BSMs off at $dx = 8$ feet.

Overflow's grid adaption capability [13] was utilized to help improve the accuracy of the solution in

critical areas. The maximum second undivided difference at each cell was chosen as the sensor function, which identifies regions that require refinement. Specifically, the value of the sensor function at each point is the maximum of 15 values: the undivided difference in each of the three grid dimensions for each of the five nondimensional states. A maximum grid size constraint of 250 million was used to balance solution accuracy and computational resources. Grid refinement was set to a maximum of two levels. The off-body adaption was limited to approximately three core diameters distance, and near body adaption was limited to the plume boxes for the cases with the BSMs on.

The original grid system had a series of handmade plume boxes, designed to resolve the BSM and core engine plumes. These plume boxes were designed to cover the entire separation trajectory, which meant certain regions were overresolved. Figure 7 shows the original grid system and solution. By utilizing Overflow's near- and off-body grid adaption to adapt to the plumes, these plume boxes can be trimmed down significantly. Figure 8 shows the adapted grid and solution. The grid adaption captures the high gradients in the plume better than the original grid topology. Additionally, the shock structure is better captured by the grid adaption.

V.   Results

The presentation of Cart3D results is divided into three categories. First, in Sec. V.A, an analysis of the full-scale Cart3D solutions along the nominal separation trajectory is presented. The subsection highlights general aspects of the flow, gives more information and visualization on the adaptive mesh, and shows the general nature of the SRB separation maneuver. Section V.B shows selected comparisons between Cart3D and Overflow solutions for a few of the cases in which both codes were run. The final subsection presents comparisons to the wind tunnel test (UPWT 1891) conducted at NASA Langley Research Center.

While giving a representative slice of the results for a database including more than 20,000 CFD solutions is necessarily challenging, this section aims to convey some of the more important information by focusing on the nominal separation trajectory. For other solutions included in the database, the boosters may be either much closer or much farther from the core, left-right symmetry is not applicable due to core sideslip angle or a failed core stage engine, and many other differences could be discussed. Many of these other families of solutions are similar in nature to those shown in this paper, but occasionally the trends in the solutions differ substantially. For further analysis of the database as a whole, see the discussion by Chan et al. [14].

Scales have been removed from the plots to satisfy project requirements regarding publication. However, in most cases the location of 0.0 on the data axis is shown, and the number of zeros shown in the label for this point gives a rough idea of the scale involved with each plot.

A.   Individual Case Results

A focus on the individual Cart3D solutions is given in this section. Figure 9 shows a close view of the forward region for one nominal BSM-on case in order to highlight the influence of the forward BSMs and also indicate the final adapted mesh resolution. Figures 10-13 highlight one case at a time for 16 of the 17 simulations on the nominal separation trajectory (the solution at dx=0 ft is not shown). The solutions are split into groups with the first group in Fig. 10 being dominated by the forward-facing BSMs, Fig. 11 showing weakening BSM influence, and cases with the BSMs off in Figs. 12 and 13. For each case, three images are shown. The first image shows a view of the core and boosters from the top. The $z = 0$ cutting plane in the first image is translucent so that the boosters, which are below the plane, can be seen. The second image shows a side view with a cutting plane at $y = 0$. In both of the pictorial figures, the colors represent static pressure divided by freestream static pressure, and all figures use the same color scale. Each slice is taken at the final time step; there is no averaging of the iterative history to make these visualizations. The third figure gives a sample of a single component/force iterative history. Side force on the right SRB is selected because that (along with the side force on the left SRB) is the most important coefficient for separation.
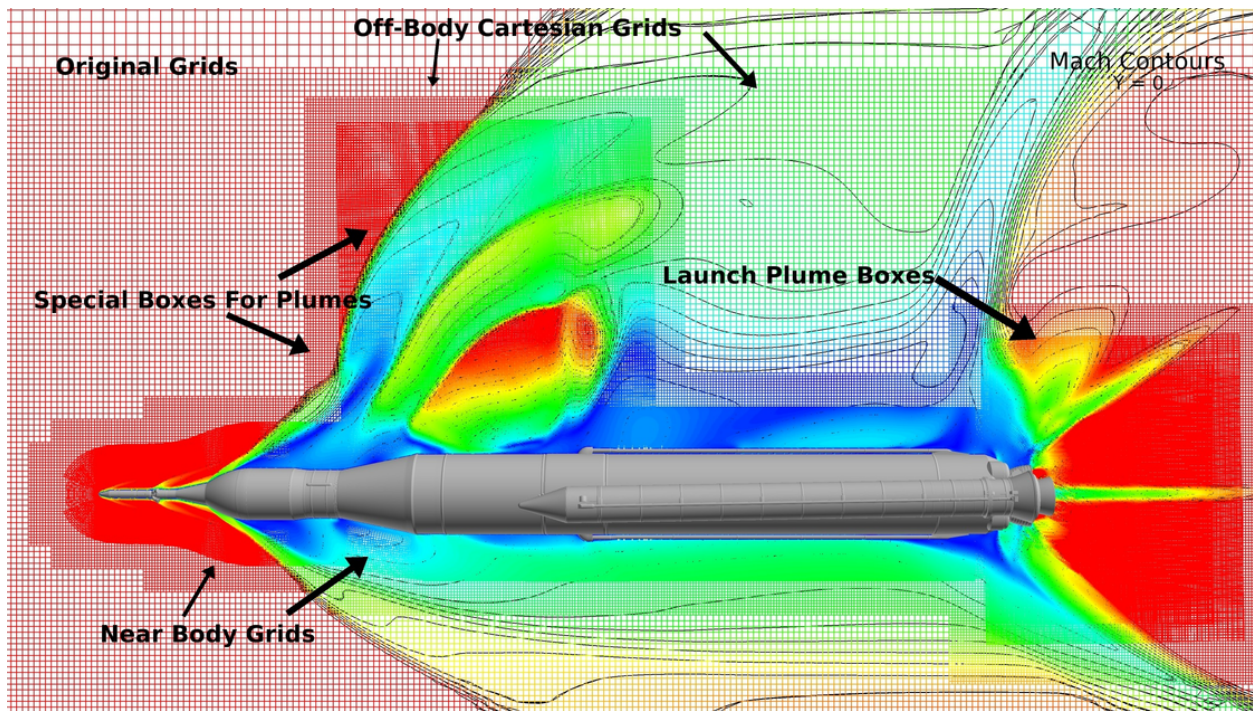
Figure 7. Manually defined Overflow SLS grid topology, with Mach contours
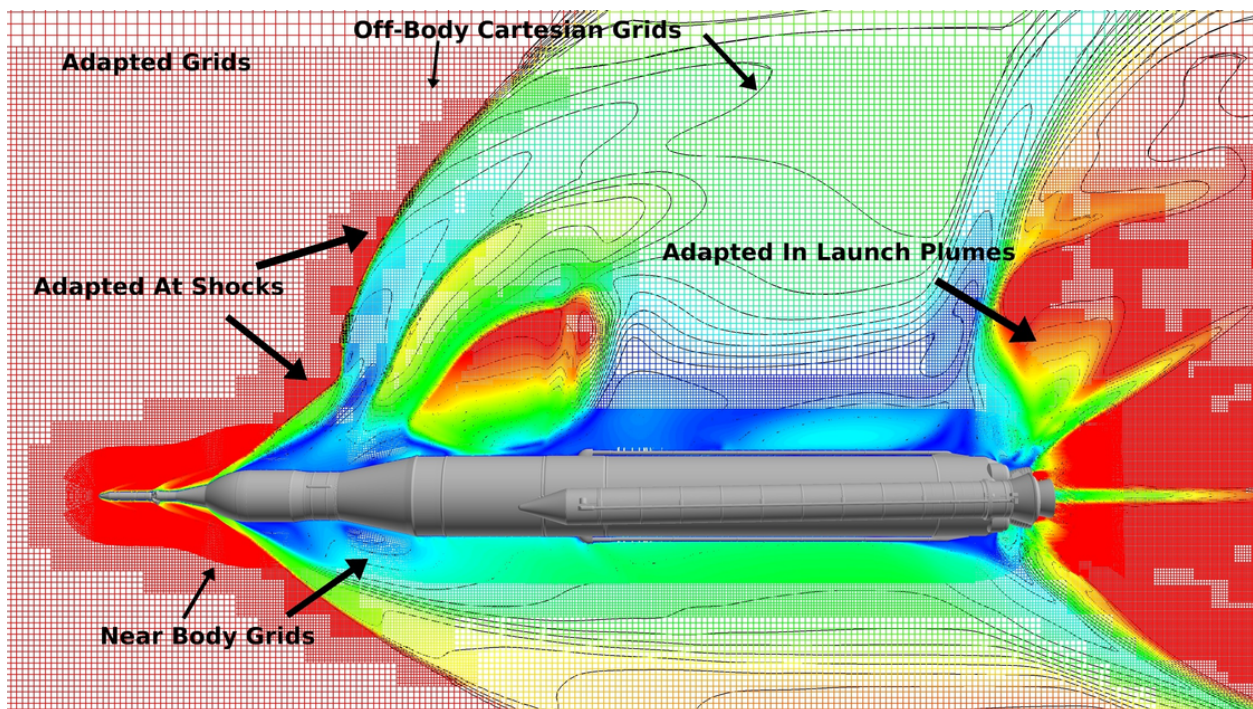
Figure 8. Adapted Overflow SLS grid topology with grid adaption, with Mach contours

American Institute of Aeronautics and Astronautics

a) Static pressure, p/p_∞, slice at $z = 0$ b) Static pressure, p/p_∞, slice at $y = 0$
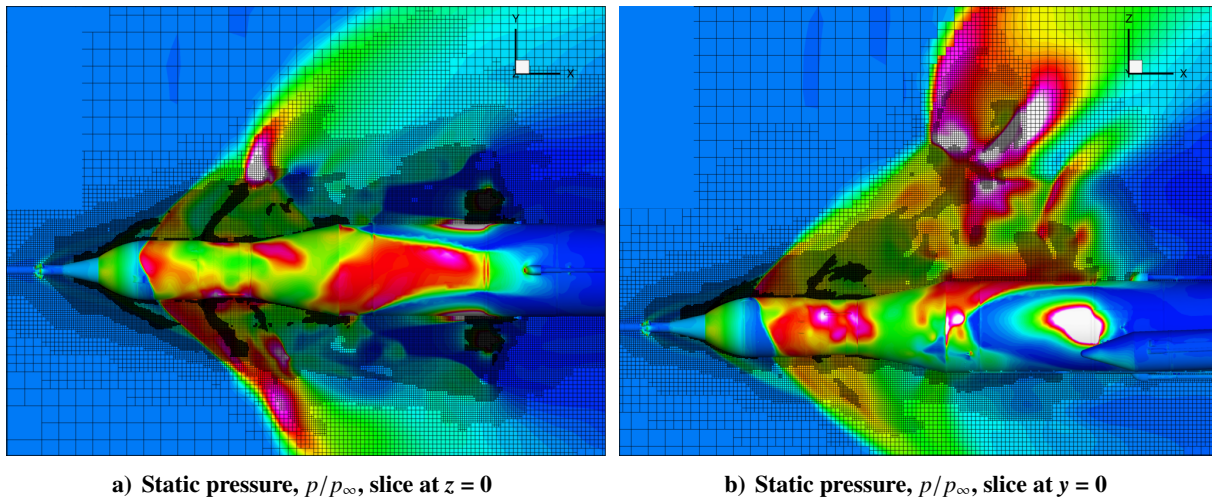
Figure 9. Forward region of *dx*=6 ft nominal BSM-on Cart3D solution

Figure 10 shows the most important solutions for determining whether or not the boosters recontact the core after separation. All four flow slices have a very similar appearance, which is not surprising because the booster positions are similar, and the BSM thrust levels are also similar. The flow is dominated by a region of high pressure near the front of the vehicle. Figure 9 provides a better view on this region by zooming in on Figs. 10g and 10h. Both images of Fig. 9 also show slices of the final mesh. The apparently black regions in Fig. 9 are actually areas of extremely high mesh density. On the side of the core there is a roughly elliptical white shape. This shows where the exhaust from the forward BSMs impinges directly onto the core, and it also highlights the partially-upstream orientation of the BSM thrust. Due to this forward-facing component of the thrust, the flow solution in this region is more interesting than it would otherwise be. The mesh adaptation procedure appropriately increases the resolution in this region aggressively, but there are obvious difficulties associated with this flow. The patchy nature of the solution suggests, correctly, that the solution is not steady, which can cause diffculties when calculating the adjoint. Furthermore, this is a case where the shock position, where the flow goes from roughly freestream pressure to much higher, shifts as the mesh is refined. Thus there are some areas with higher resolution than necessary. At first this may seem a little disappointing, but in reality it is remarkable that a single Haswell node with 24 cores and 128 GB of memory can solve such a complex geometry and flow topology in just two hours.

The RSRB side force histories in Fig. 10 show that on the coarser meshes before iteration 2500, the flow is basically steady. Then, on the final mesh, there are many more fluctuations. The red dashed lines are shown to give a common reference scale, and the blue rectangle shows the domain over which the database force coefficient was averaged. The height of the blue rectangle is one standard deviation of the force history over the iterations used for the average. Although the four solutions in Fig. 10 have many nominal similarities, the integrated forces and moments show larger differences. A large driver of the integrated forces and moments is the impingement of the core engine thrust on the aft end of the boosters. Because the engine exhaust has such a high pressure, the small area of interaction between core engine exhaust can contribute more than half of the entire force on the booster. Furthermore, it is difficult to predict the extent of this interaction, and so creating such a large database is necessary to resolve the boundaries.

Figure 11 shows snapshots of the nominal trajectory along the transitional region, which is highlighted by a gradual decrease in the BSM thrust. The difference between the solutions at 10 ft and 15 ft in particular shows how much the flow is affected by changes in the level of BSM thrust. Between the two figures, the booster position is just slightly different, but the flow solution is quite different. Then by 20 ft and 25 ft, the effect of BSMs is less and less noticeable. In Fig. 11k, the influence of the forward BSM thrust is still slightly visible, mostly as a a yellow dot about half way down the length of the core. The iterative histories

American Institute of Aeronautics and Astronautics

a) *dx*=2 ft   b) *dx*=2 ft   c) **RSRB side force history**

d) *dx*=4 ft   e) *dx*=4 ft   f) **RSRB side force history**
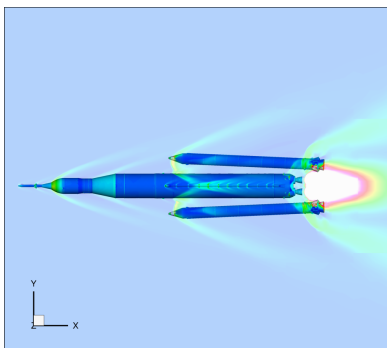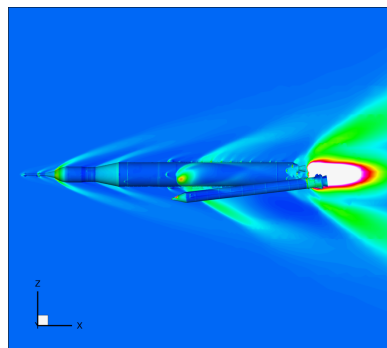
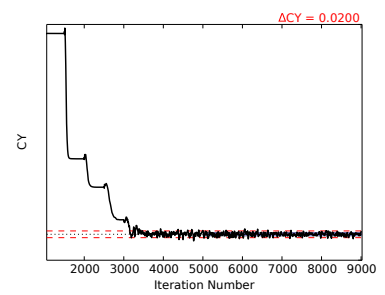g) *dx*=6 ft   h) *dx*=6 ft   i) **RSRB side force history**

j) *dx*=8 ft   k) *dx*=8 ft   l) **RSRB side force history**
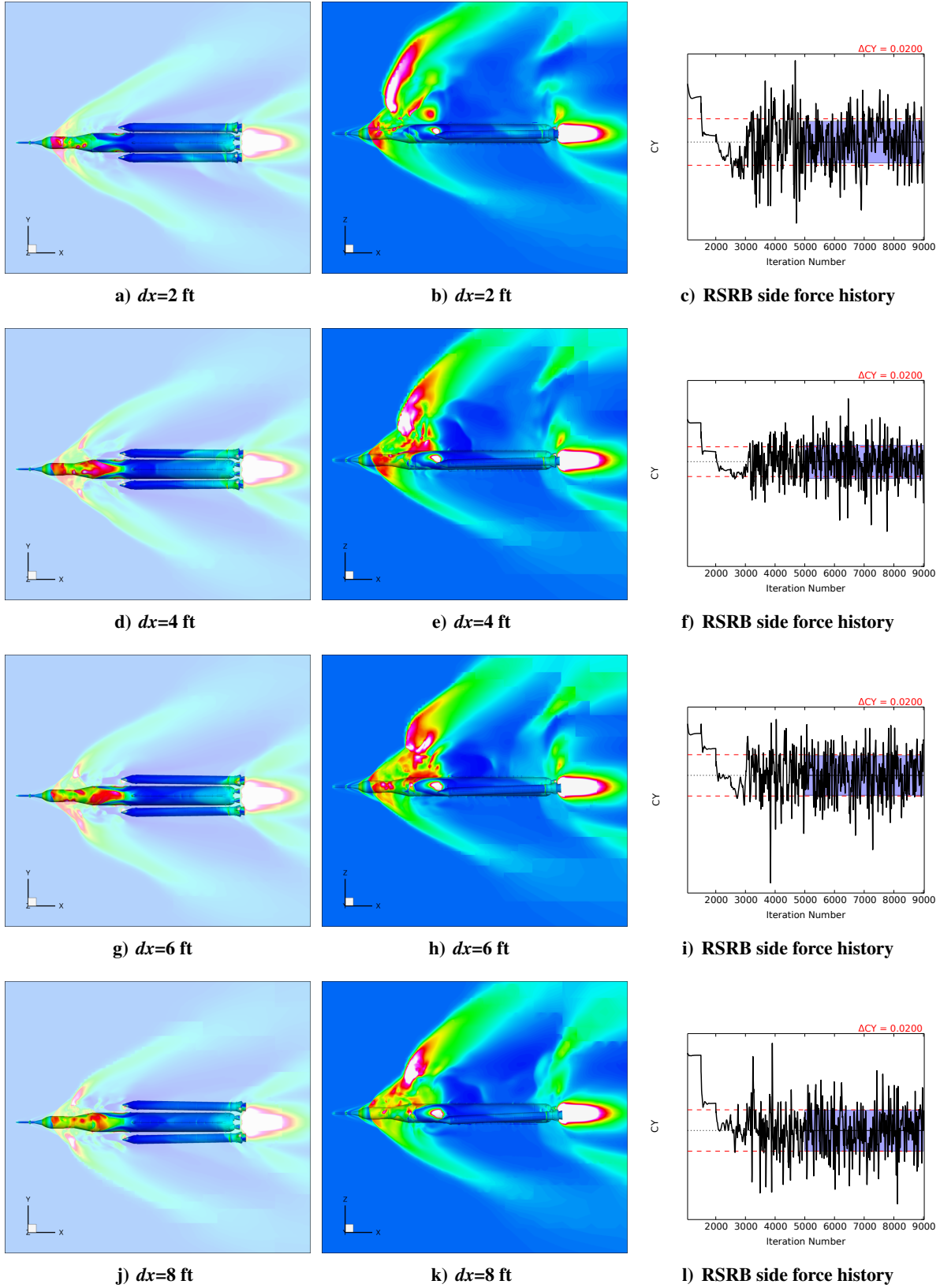
Figure 10. Top view and pitch plane of Cart3D static pressure slices for nominal trajectory

American Institute of Aeronautics and Astronautics
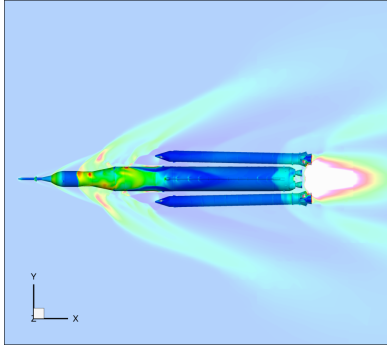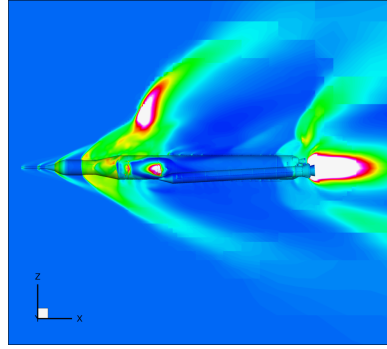
a) *dx*=10 ft

b) *dx*=10 ft
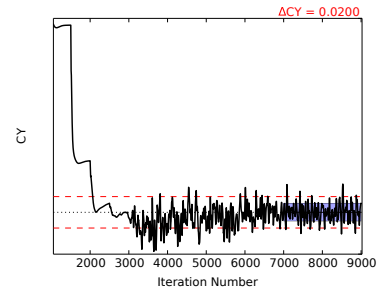
c) RSRB side force history
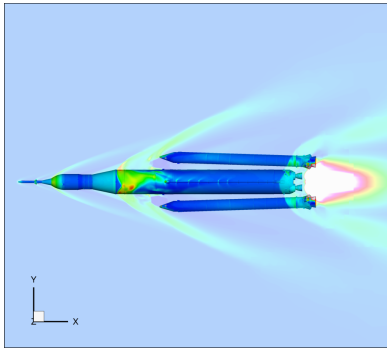
d) *dx*=15 ft
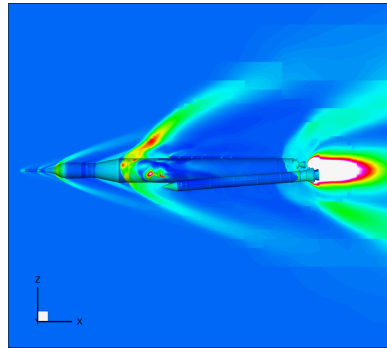
e) *dx*=15 ft
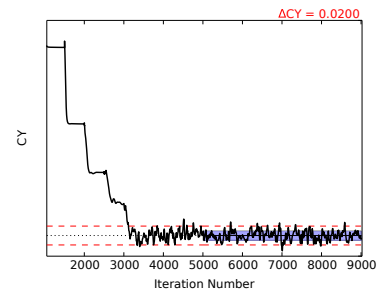
f) RSRB side force history
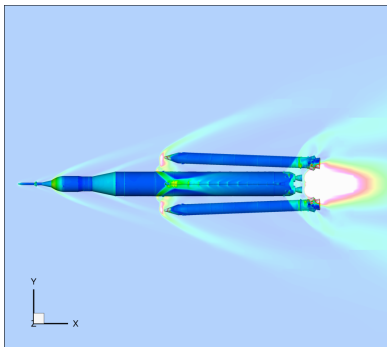
g) *dx*=20 ft
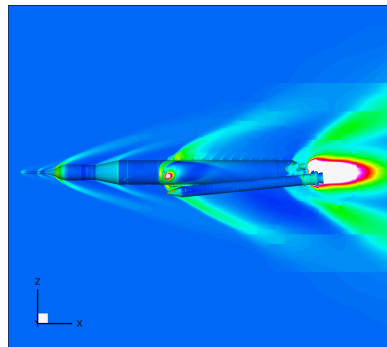
h) *dx*=20 ft
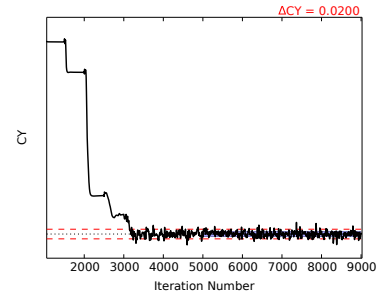
i) RSRB side force history

j) *dx*=25 ft

k) *dx*=25 ft

l) RSRB side force history

Figure 11. Top view and pitch plane of Cart3D static pressure slices for nominal trajectory

in Fig. 11 show decreasing fluctuation magnitudes corresponding to this thrust tail-off, but it is somewhat difficult to determine from the figures because there is a corresponding increase in the magnitude of *CY*. As the boosters move further aft, more and more of the tail portions of the boosters move into the core engine exhaust plumes, which tends to increase the magnitude of integrated force and moment coefficients.

In Fig. 12, the BSMs are no longer firing, and the solutions show fewer features in general than the previous figures. The most interesting aspects of the flow are the interactions between the aft portion of the SRBs and the core engine exhaust plume. Figures 12e and 12j in particular show a lot of features on the aft surfaces of the boosters. Also in Fig. 12, the force fluctuations on the final mesh are either gone or much smaller than in previous figures. Without the distractions from fluctuations, the grid convergence behavior is also easier to observe. The penultimate mesh is used for iterations 1600 to 2000, and the final mesh is used for iterations 2000 to 3000. Except for Fig. 12f, the value for *CY* is consistent between these last two meshes. On the first two meshes (up to iteration 800), the mesh is quite coarse in some regions, and the value seems dramatically different from subsequent results. This is partially the consequence of trying to use common inputs for the entire separation database to avoid jumps in results. Specifically, the forward region of the core has higher resolution than necessary in the Fig. 12. When appropriate, the adaptation procedure adds more cells in the region where the SRBs interact with the core engine plumes.

Figure 13 shows results very similar in nature to those of Fig. 12, except that the boosters have moved even further aft. Because the boosters are being impinged upon by the core engine plumes, the aerodynamic forces on the boosters can be as much as 100 times larger than the corresponding values from the solutions in Fig. 10. In light of the wide range of configurations, and considering the necessary computational efficiency to analyze so many configurations, the combination of Cart3D and this run strategy was highly successful.

B.   Code-to-Code Comparisons

One of the key sources of confidence in the booster separation aerodynamic database comes from comparisons of the Cart3D results with higher-fidelity results from the viscous Overflow code. Comparisons with physical experiments is the ultimate source of confidence in such models, and a discussion of wind tunnel results is presented in Sec. V.C. The complexity of this configuration, range of scales involved, and number of cases required to analyze suggested the three-legged approach to verification and validation discussed here. A simplified explanation of this approach is that the experimental comparisons provided the highest degree of confidence while the code-to-code comparison is easier to interpret. Because neither of the three data sources is a perfect representation of reality, the uncertainty database contains contributions from both the code-to-code comparison and the Cart3D-to-wind tunnel comparison.

Figures 14-17 show comparisons between Cart3D (black) and Overflow (red) for four slices of the nominal separation trajectory. In each figure circles are used for integrated and averaged forces or moments on the core, right-facing triangles are for the right SRB, and left-facing triangles are for the left SRB. The blue bands show one standard deviation of the Cart3D iterative history of the corresponding coefficient, which is the same as the height of the blue rectangles in Figs. 10-13. The darker blue areas represent overlap of the one-sigma bounds of the left and right boosters. This measure is only one of the contributors to the uncertainty, and furthermore, the uncertainties are based on three-sigma distributions. These one-sigma bounds in blue are used to give the reader an idea of the relative sizes of Cart3D-to-Overflow differences and the intrinsic uncertainty of the steady-state inviscid simulations. In each of images of Figs. 14-17, the numbers and tick marks on the *y*-axis have been removed. The location of the zero axis has been retained, and the number of zeros shown after the decimal place shows the order of magnitude of the results.

Figure 14 shows the most important results of the entire database. Any post-separation recontacts between the core and SRBs would occur in the first ten feet of axial separation, and aerodynamic uncertainty in this region has been an important factor in the design review of the entire vehicle. Furthermore, the aerodynamic forces on the boosters play a far more significant role than the aerodynamic forces on the core for two reasons: the partially-fueled core has much more inertia than the burnt-out SRBs, and the core is under active control while the boosters are not. Figures 14c and 14d show the most important coefficients
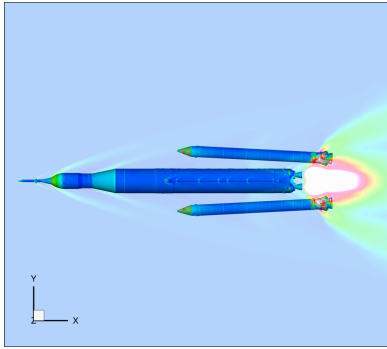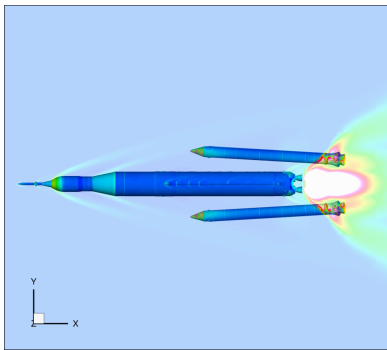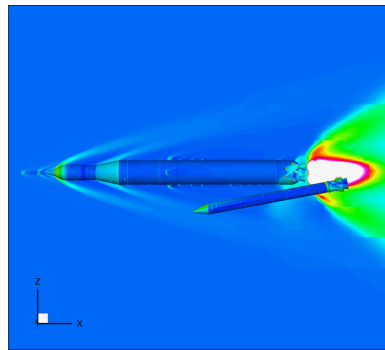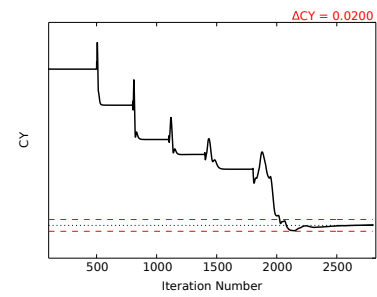
a) *dx*=35 ft
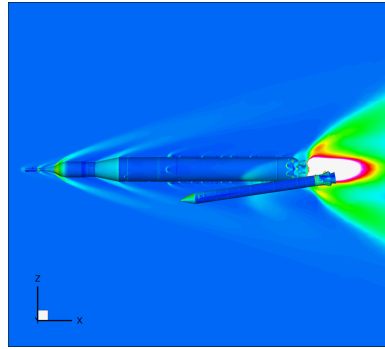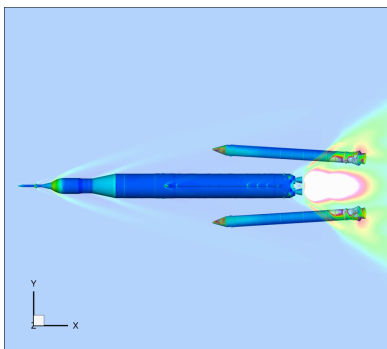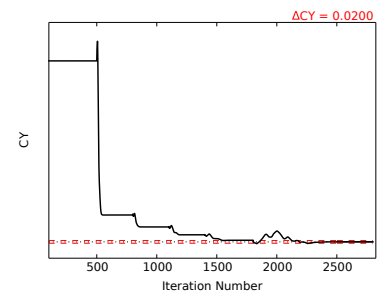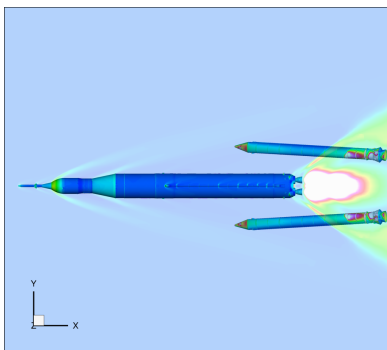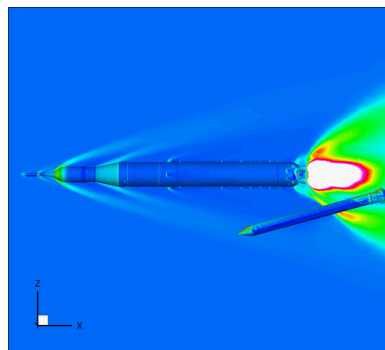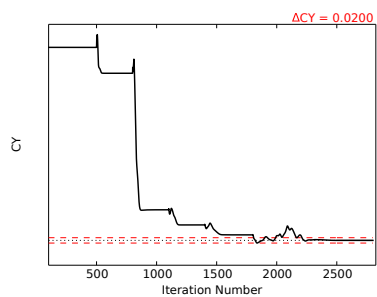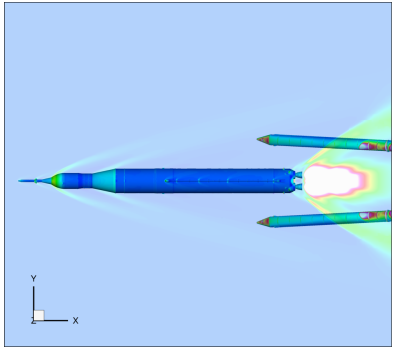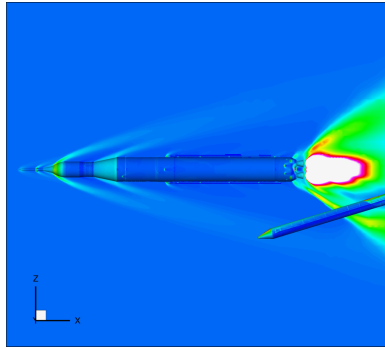
b) *dx*=35 ft
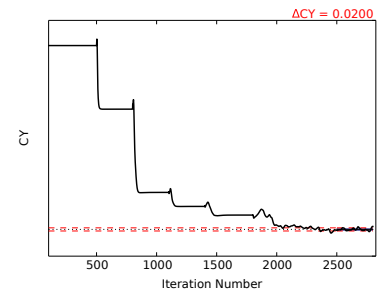
c) **RSRB side force history**

d) *dx*=50 ft

e) *dx*=50 ft

f) **RSRB side force history**

g) *dx*=75 ft
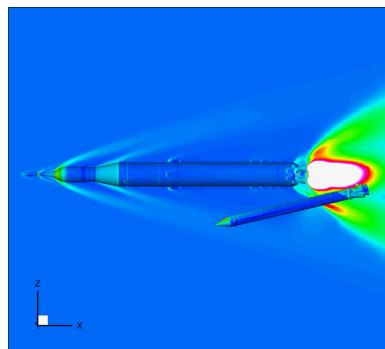
h) *dx*=75 ft

i) **RSRB side force history**

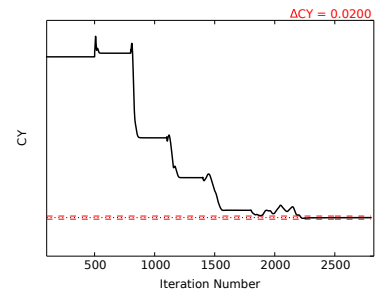j) *dx*=100 ft

k) *dx*=100 ft

l) **RSRB side force history**

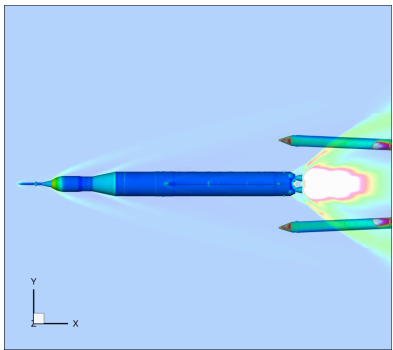**Figure 12. Top view and pitch plane of Cart3D static pressure slices for nominal trajectory**
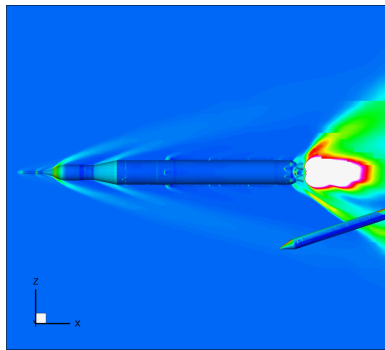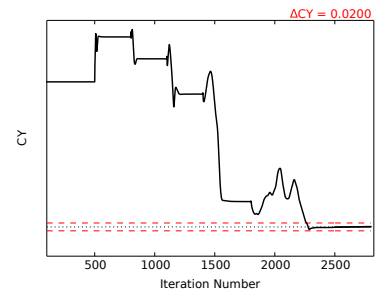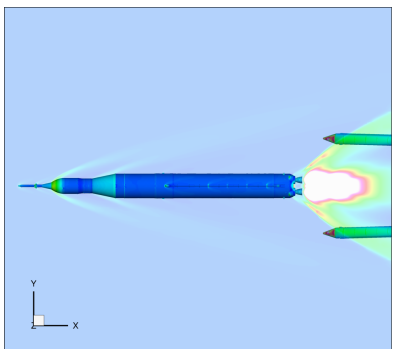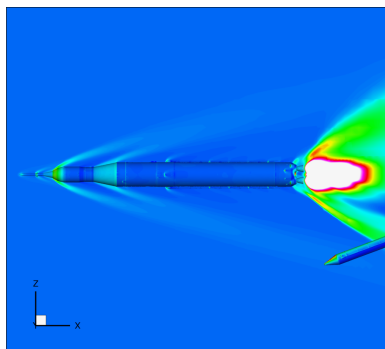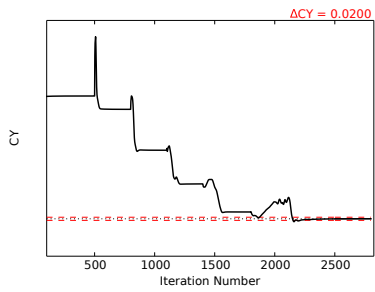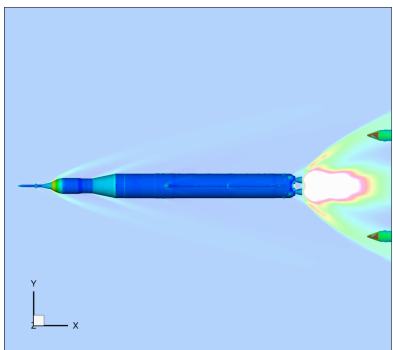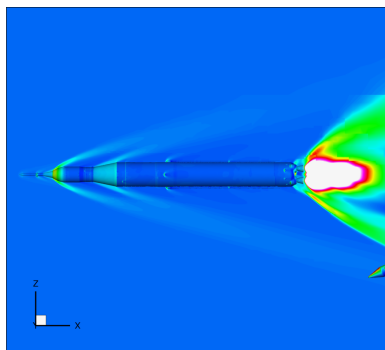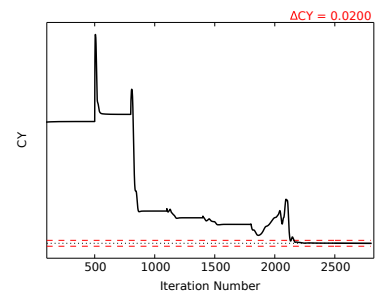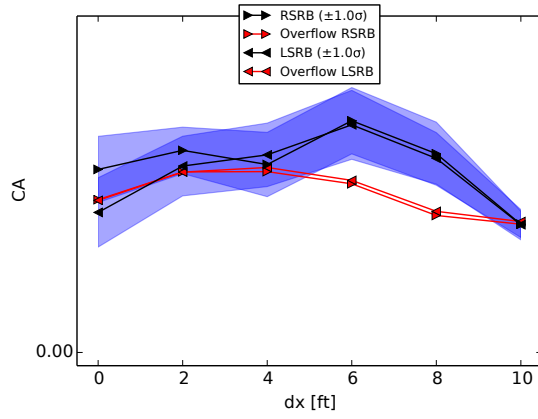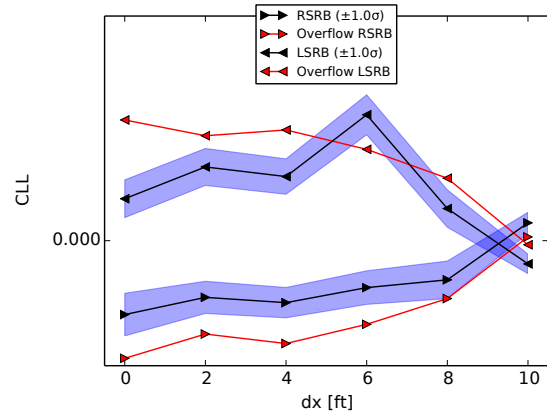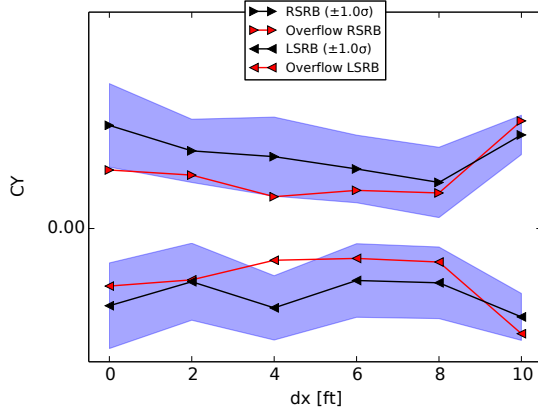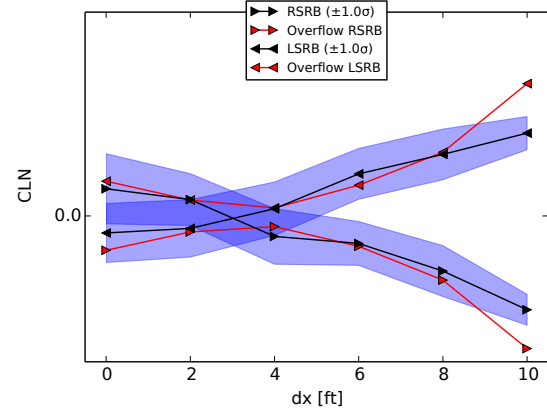
a) *dx*=125 ft

b) *dx*=125 ft

c) RSRB side force history

d) *dx*=150 ft

e) *dx*=150 ft

f) RSRB side force history

g) *dx*=200 ft

h) *dx*=200 ft

i) RSRB side force history

j) *dx*=250 ft

k) *dx*=250 ft

l) RSRB side force history

Figure 13. Top view and pitch plane of Cart3D static pressure slices for nominal trajectory
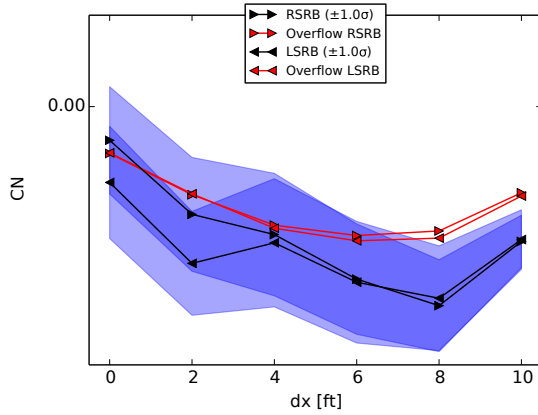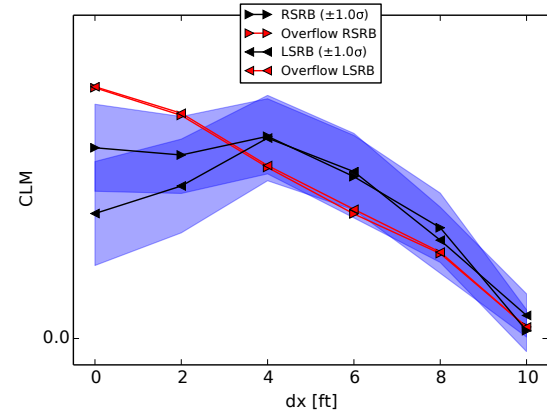
a) Axial force, *CA*

b) Rolling moment, *CLL*

c) Side force, *CY*

d) Yawing moment, *CLN*

e) Normal force, *CN*

f) Pitching moment, *CLM*

Figure 14. Comparison between Cart3D and Overflow SRB forces and moments for nominal separation trajectory

for evaluating the success of the separation. A trajectory analysis using a much earlier booster separation aerodynamic database (with about 300 Cart3D solutions) determined that these were the most critical coefficients by turning off the uncertainty of each coefficient individually. The results in Fig. 14c show that the two codes predict similar results. Nevertheless, due to the very small magnitude of the force coefficient itself, the uncertainty is still about 100%. This is both somewhat misleading and more acceptable than it seems; previous uncertainties on this coefficient were more like 500% to 1000% of the size of the force. Carefully selected Cart3D inputs and improvements in the mesh adaptation technology played a role in reducing this uncertainty, but another major contributor came from having many more Cart3D and Overflow solutions. This discussion of just one coefficient of just six of the 20,000 solutions in the database demonstrates how simply obtaining more data was the most critical factor in delivering acceptably small aerodynamic uncertainties. Obtaining a perfect solution for perhaps 200 cases would not result in a small uncertainty because it would not adequately capture the trends in the database. In fact, even with the multitude of Cart3D solutions used to assemble this database, the largest or second largest contributor to the combined uncertainty was interpolation error between the Cart3D solutions. For information about the determination of the database uncertainties, see [14].

The other results of Fig. 14 have similar trends, although the normal force and pitching moment tend to show closer agreement than the side force and yawing moment. The axial force on the booster shows quite close agreement. In this case, the complex flow from the BSM exhaust results in the direct viscous influence being difficult to spot, but a more typical viscous increment is found in later figures. Finally, the rolling moment shows a bit more sporadic behavior, but the size of these moments are so small that the differences do not register as worrisome.

Figure 15 shows the integrated forces and moments on the core for the BSM-on cases. This includes the first 10 ft shown in Fig. 14 plus three more solutions out to 25 ft. The reason these results between 10 ft and 25 ft are excluded from Fig. 14 is that the core engine exhaust causes much larger forces and moments in this region that make the critical differences within the first 10 ft difficult to see. The major trend in the BSM-on results for the core is caused by shifts in the BSM-on thrust. The lateral force (CY) and yawing moment (CLN) show the expected left-right symmetry for this configuration at zero sideslip, although Overflow gives a more consistent prediction than Cart3D for the first 10 ft. The axial force again shows acceptable agreement, and then the viscous increment between Overflow and Cart3D is visible from 15 ft onward after the BSM-on thrust begins to tail off. Like before, the rolling moment is very small. In the pitch plane, there is a more significant difference between Cart3D and Overflow in the first 10 ft. Despite a Cart3D overprediction of the downward normal force and pitching moment by up to 100%, this actually demonstrates closer agreement than what was discussed in [7]. Viscous effects in this region of the database probably limit the accuracy of inviscid steady-state simulations. Further efforts to improve the agreement was ceased as these two coefficients are not critically important for separation.

The BSM-off integrated forces and moments are plotted in Figs. 16 and 17. The SRB forces and moments in Fig. 16 are mostly dominated by the effects of core exhaust, which makes the high degree of agreement between the two codes more impressive. Cart3D simulated the core engine exhaust as high-temperature air, while Overflow used a specific heat ratio more representative of the actual engine exhaust. Further discussion of this modeling assumption and its effects can be found in [15]. Since the forces and moments on the SRBs in these plots are strongly affected by the core engine exhaust and its expansion, these results give an affirmation of the Cart3D exhaust modeling procedure discussed more in [7] and originally proposed in [4].

Without the influence of the BSMs, the typical viscous increment between Cart3D and Overflow can be seen in Fig. 17a. The rolling moment, lateral force, and yawing moment in Fig. 17 should all be close to zero due to the symmetry of the problem, and the results of both Cart3D and Overflow are consistent with this prediction. In the first 25 ft, the data appear jagged, but the scale is small enough that this is an expected result. Figures 17e and 17f give an example that demonstrates the need to include so many cases in the database; shocks from the SRB interact with the core body to cause a positive normal force and
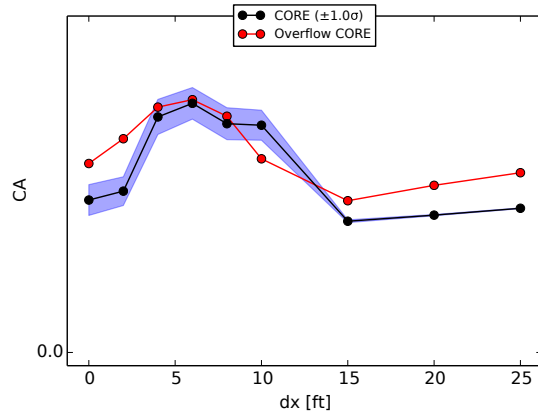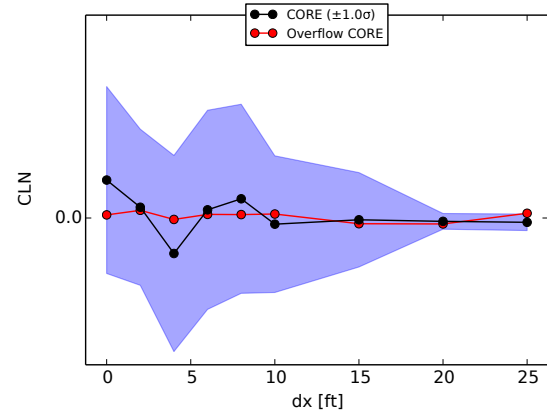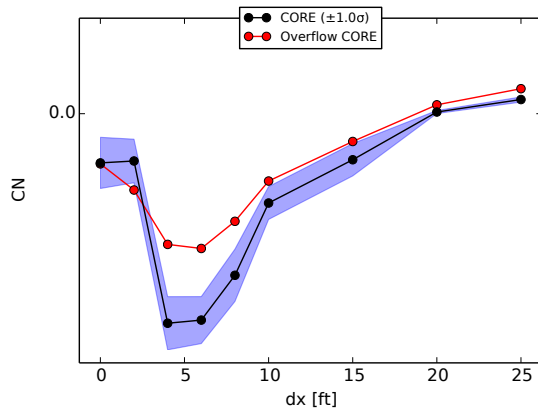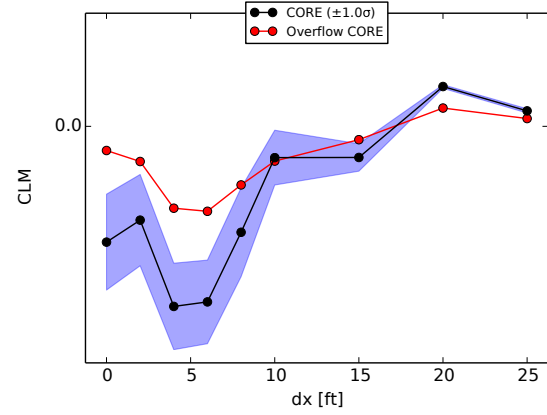
a) **Axial force, *CA***
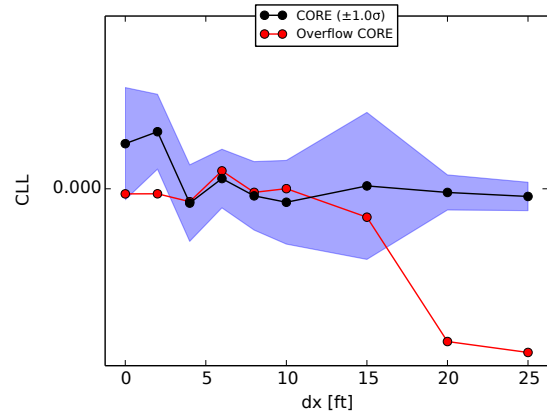
b) **Rolling moment, *CLL***
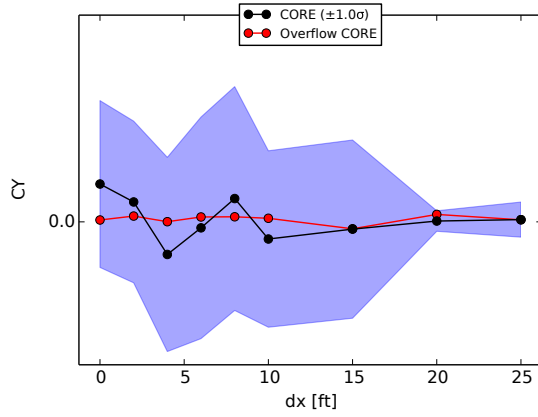
c) **Side force, *CY***
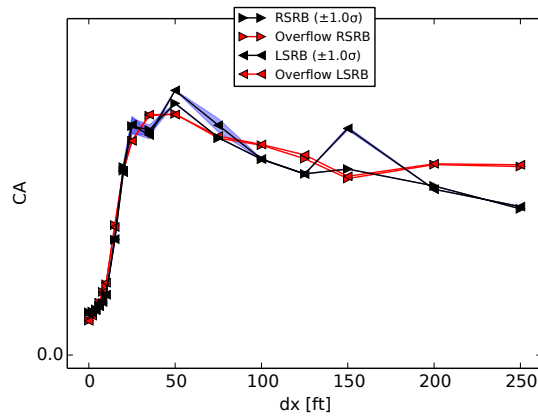
d) **Yawing moment, *CLN***
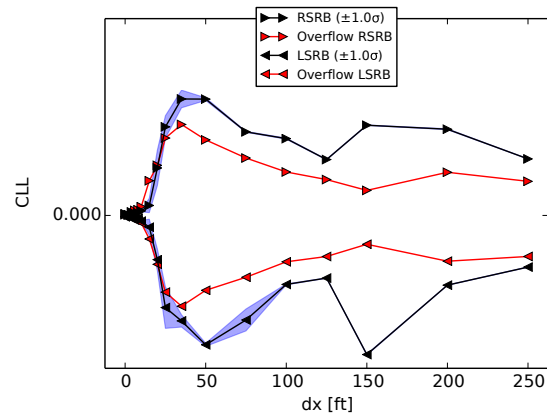
e) **Normal force, *CN***

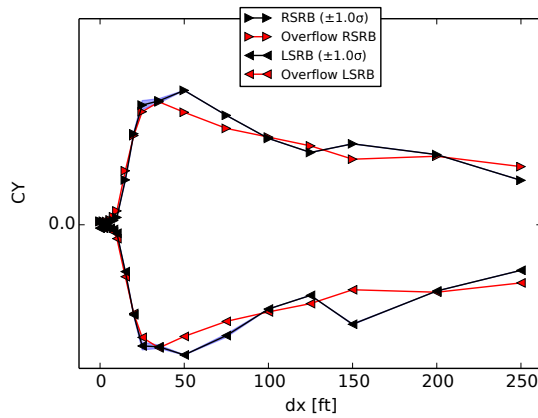f) **Pitching moment, *CLM***

Figure 15. Comparison between Cart3D and Overflow forces and moments on the core for nominal separation trajectory

a) Axial force, *CA*

b) Rolling moment, *CLL*

c) Side force, *CY*

d) Yawing moment, *CLN*

e) Normal force, *CN*

f) Pitching moment, *CLM*

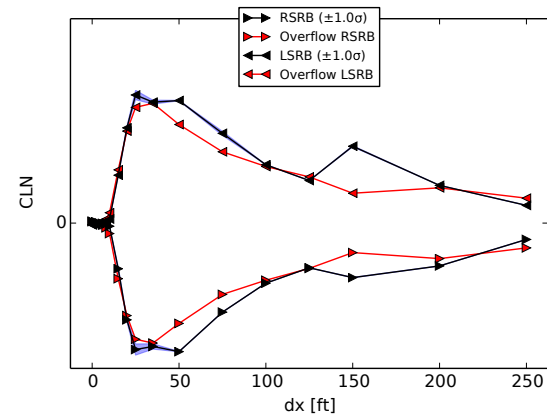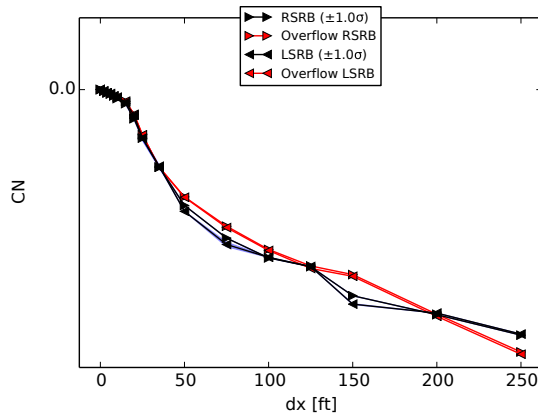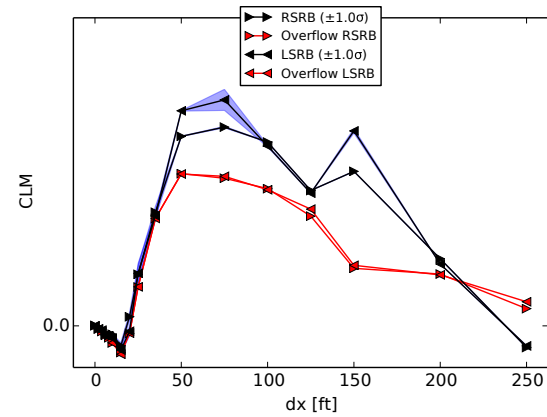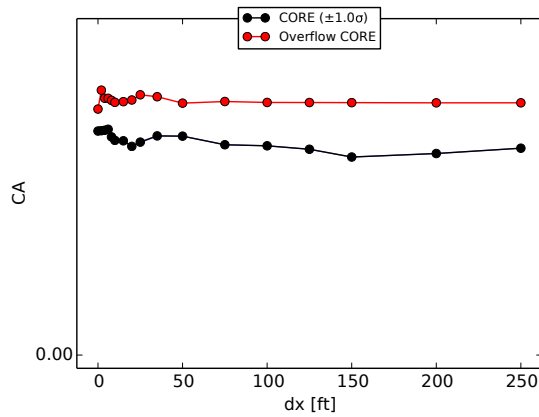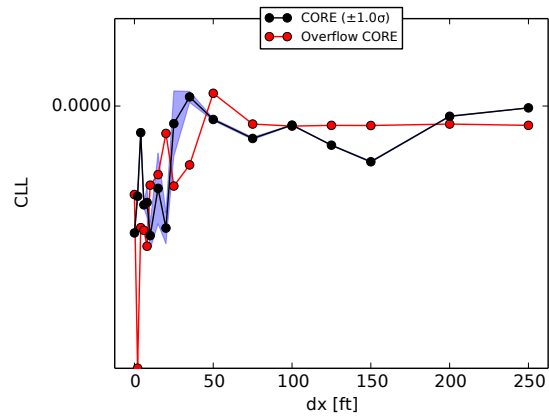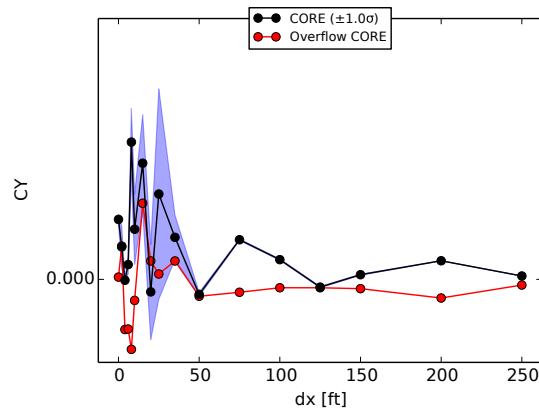**Figure 16. Comparison between Cart3D and Overflow SRB forces and moments for nominal separation trajectory with BSMs off**

a) Axial force, *CA*

b) Rolling moment, *CLL*

c) Side force, *CY*

d) Yawing moment, *CLN*

e) Normal force, *CN*

f) Pitching moment, *CLM*

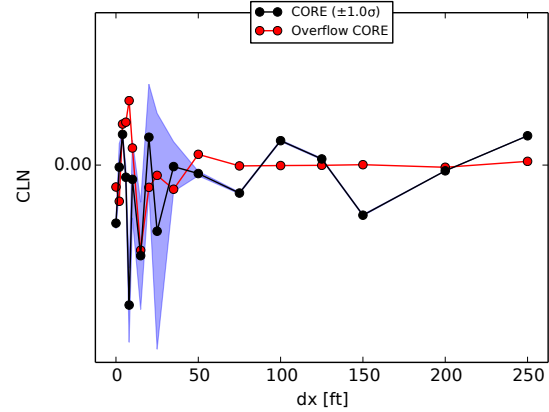**Figure 17. Comparison between Cart3D and Overflow forces and moments on the core for nominal separation trajectory with BSMs off**
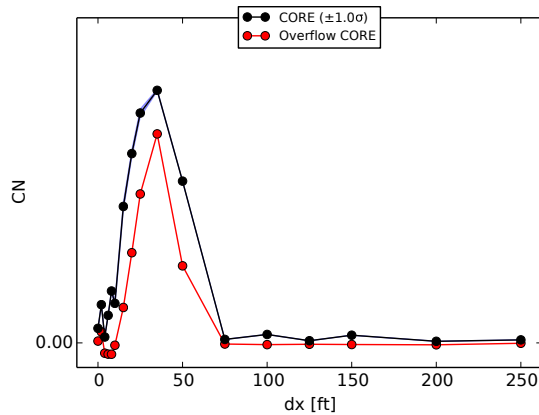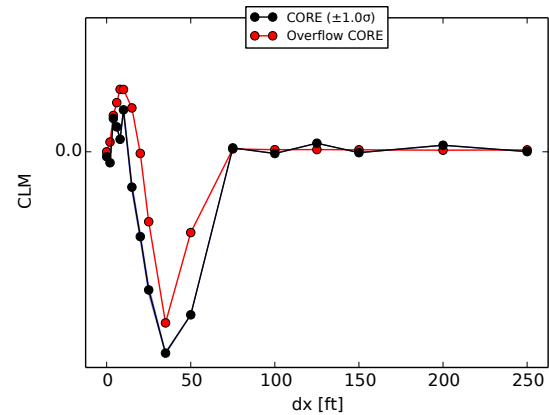
a) Surface geometry without support hardware **b) Surface geometry including support hardware**
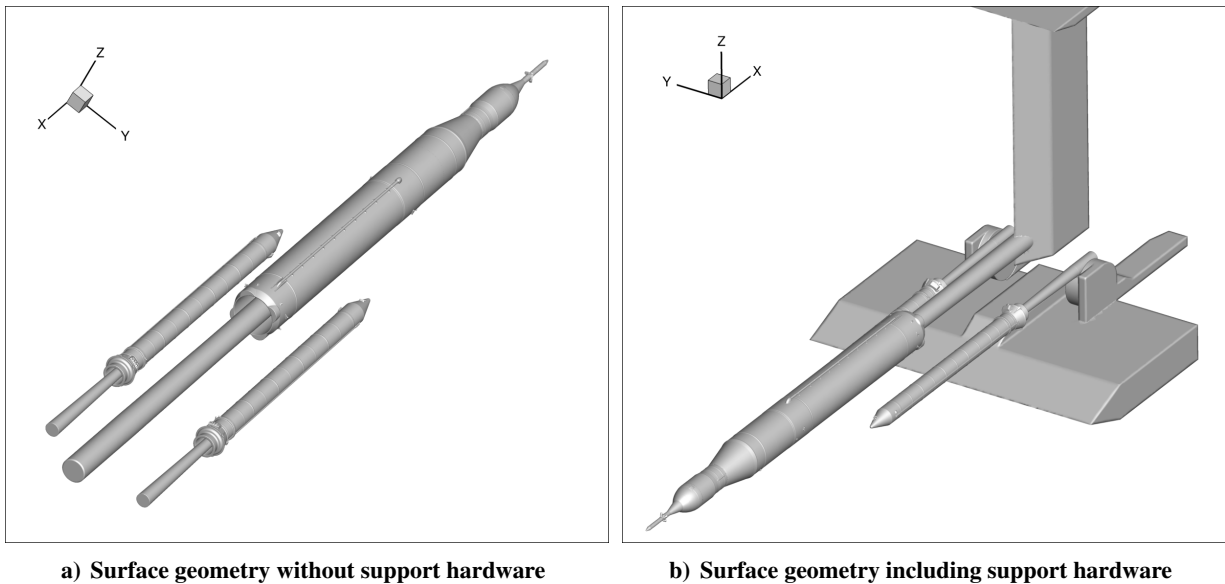
Figure 18. Surface geometries for Cart3D analysis of wind tunnel test

nose-down moment for a relatively small portion of the database. Using a coarser database makes missing sharp features like this more likely, and the database probably misses some smaller features even with the thousands of simulation that were included.

Overall, the agreement between Overflow and Cart3D in Figs. 14-17 is consistent and acceptable. Since Overflow was run for about 250 cases, there are about ten times as many figures that could be shown with similar results. The other results show a similar level of agreement between the two codes. In general, better agreement is observed when the boosters are farther from the core than the nominal trajectory, and slightly worse agreement is observed when the boosters are closer to the core.

C. Comparison to Wind Tunnel Test

In September through November of 2014, a wind tunnel test was conducted at NASA Langley Research Center's Unitary Plan Wind Tunnel (UPWT) to help understand the performance of SLS booster separation [11]. BSM thrust was simulated using air while core engine exhaust and SRB exhaust was not modeled. All three bodies were independently movable, as shown in the surface geometry in Fig. 18.

A separate surface grid was created in order to simulate the wind tunnel configuration directly and obtain code-to-experiment contributions to the overall uncertainty of the database. Approximately 6000 Cart3D simulations were computed in order to uncover as many trends in the differences as possible. One detraction from this effort is that the small size 0.9% scale of the wind tunnel model effectively prohibited obtaining many solutions corresponding to the critical first moments of the separation maneuver.

However, the comparison showed generally good agreement between Cart3D and the experimental results. Unlike the order of results presented in this paper, the wind tunnel configuration was the first one analyzed by Cart3D. Therefore acceptable comparison to the experimental results was used as a filter before continuing with analysis of the flight-scale vehicle. Had the results been less agreeable, an alternative approach would have been needed. Possible alternatives would have included accepting the high aerodynamic uncertainties, using a more expensive CFD approach, conducting a larger and more expensive wind tunnel test, or making changes to the vehicle design.

Figures 19 and 20 show a small subset of these Cart3D solutions alongside the corresponding experimental measurements. The Cart3D results are shown in black, and the wind tunnel measurements are red. Experimental results are not present in Figs. 19a and 19b because those two coefficients were not measured

in the experiment. During the experiment, data was collected in sweeps in which the axial displacement of the boosters (dx) was increased while the other variables were kept roughly constant. The axes are labeled with (dxR) because the left and right boosters did not have exactly the same position; the results are plotted against position of the right booster. Finally, the wind tunnel test was conducted with a 0.9% scale model, and so the data corresponding with the critical first 10 ft of separation for the flight database is within the first 1.08 in of the experimental data.

Although Fig. 19 shows some localized differences between the inviscid simulations and the experimental data, the absolute agreement is remarkably good. Figures 20e and 20f show that Cart3D predicts a small jump in the data at around 3 inches which is not present in the experimental data. This is caused by a change in the prediction of the shock position induced by the forward BSMs, and the effects are more visible in Fig. 20. Fortunately, there is no corresponding flight condition with such a large value of dx while the BSMs are still firing. Since the SRB forces and moments were known to be the most important outputs of the aerodynamic database, results like these gave the team confidence to proceed with the flight-scale database. There are roughly 70 other analogous plots for other sweeps of experimental data; the agreement of Figs. 19 and 20 is representative of the other results.

The integrated core forces and moments from the same set of conditions is shown in Fig. 20. Agreement is generally good for these results, although the figures demonstrate that the coefficients tend to not change much as a function of dxR as the main trend in most of the figures is flat. Figure 20a shows some change in the nature of the inviscid solutions around 3 inches that is not present in the wind tunnel data. This jump is caused by a shift of the forward shock location, while Schlieren imagery from the wind tunnel test indicate the shock does not shift as the boosters translate aft. Other data sweeps show worse agreement in *CN* and *CLM*, which matches the discussion of Sec. V.B. Interestingly, it appeared that the Cart3D-to-Overflow and Cart3D-to-experiment differences in these two coefficients were very similar. Thus counting both sets of differences in the uncertainty is conservative, but since no Overflow simulations were performed on the wind tunnel geometry, there was no attempt to take advantage of such observations. If it is determined that even smaller aerodynamic uncertainties are essential for flight, this is one area that can be targeted for improvement.

VI.   Conclusions

This paper discussed a computational aerodynamic database that involved a high degree of complexity and required a careful balance between computational accuracy and number and placement of solutions. While a limited number of high-fidelity solutions would not be adequate, the close tolerances involved in booster separation indicate that a huge number of low-fidelity solutions would also not be satisfactory. The approach presented here sought to strike an appropriate balance between these competing requirements, and an internal NASA review process to certify the database is underway.

Regarding the generation of similar aerodynamic databases for problems with jet interaction, significant lessons were learned. Especially if there are any nozzles whose thrust directions have an upstream component, there may be multiple categories of solutions from any one solver. While a mesh convergence study is always a recommended practice, complex configurations such as the SLS booster separation benefit immensely from investigating mesh resolution and sensitivity to other inputs. Specific lessons included uses of output-based mesh adaptation in simulations without adequate primal convergence, distributing resolution appropriately for complex geometries with a wide range of scales, and development of robust inputs to minimize the number of manual operations for such a large database. The database also provided insights into combining multiple imperfect data sources to create both an aerodynamic database and an uncertainty distribution for a vehicle that must be certified for human crews. Furthermore, a carefully selected run matrix can be critical to the successful implementation of a database even if the individual computations are nearly perfect.

Coordination with the rest of the SLS team has indicated that the aerodynamic database and uncertainties based on this work results in a successful separation. Finally, uncertainty quantification has identified
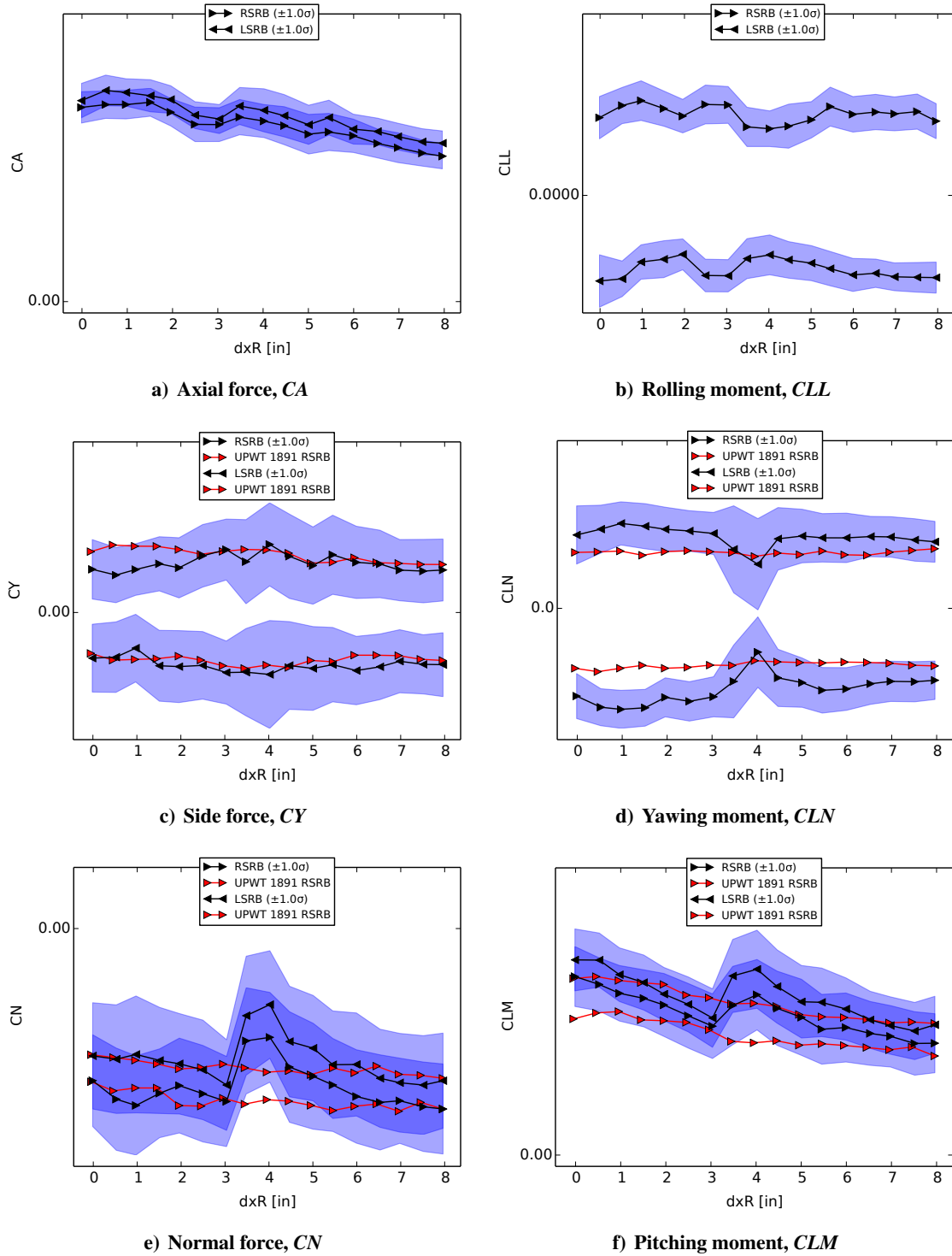
a) Axial force, *CA*

b) Rolling moment, *CLL*

c) Side force, *CY*

d) Yawing moment, *CLN*

e) Normal force, *CN*

f) Pitching moment, *CLM*

Figure 19. Comparison between Cart3D and wind tunnel (UPWT 1891) forces and moments on the SRBs for one *dx* sweep. Standard deviation of Cart3D iterative history shown in blue.
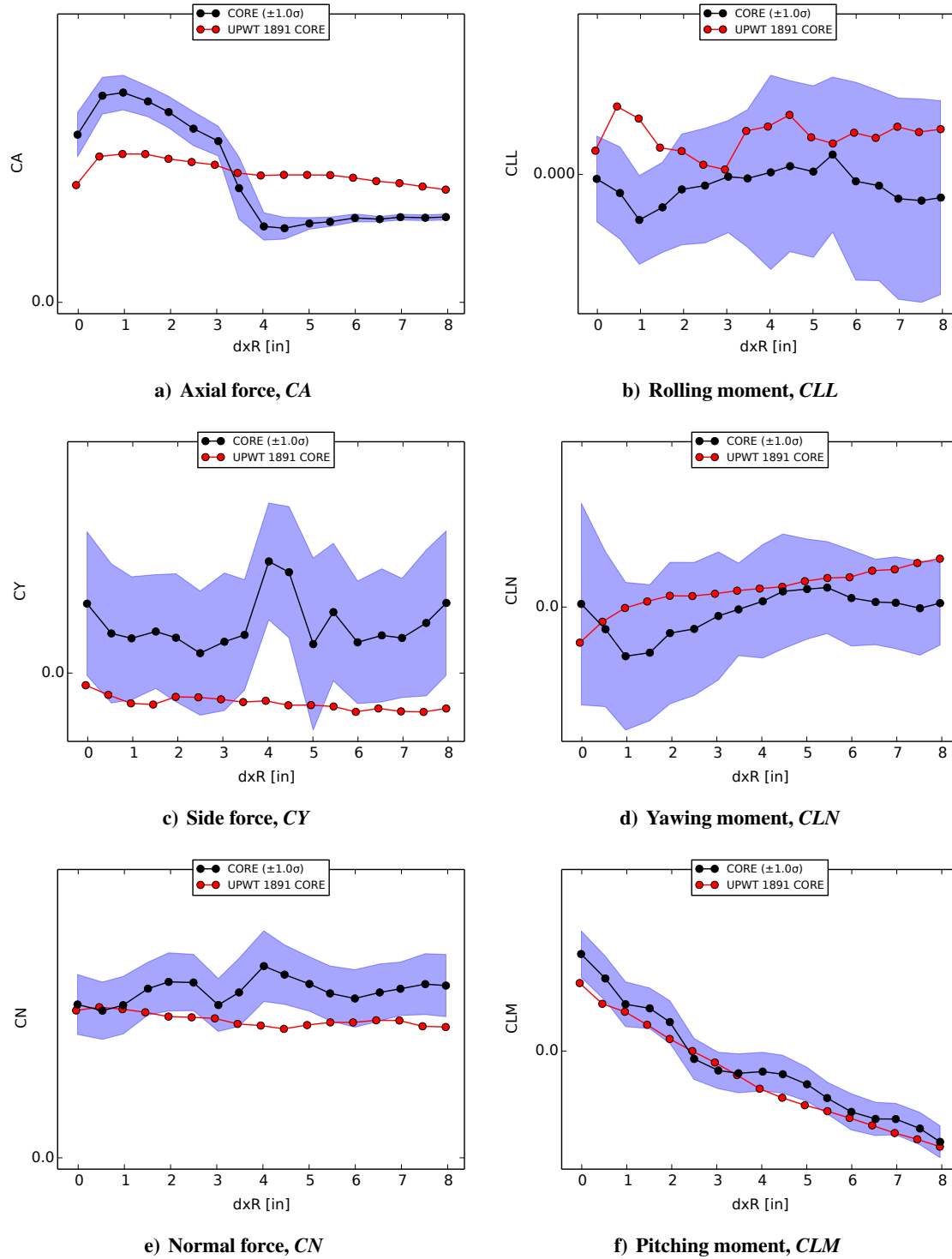
American Institute of Aeronautics and Astronautics

a) Axial force, *CA*

b) Rolling moment, *CLL*

c) Side force, *CY*

d) Yawing moment, *CLN*

e) Normal force, *CN*

f) Pitching moment, *CLM*

Figure 20. Comparison between Cart3D and wind tunnel (UPWT 1891) forces and moments on the core for one *dx* sweep. Standard deviation of Cart3D iterative history shown in blue.

interpolation as the largest contributor to aerodynamic uncertainty. This indicates that the balance between accuracy and efficiency selected for this work was appropriate, and the most effective way to reduce uncertainty is to simulate more cases using the same strategy.

Acknowledgments

References

[1] Aftosmis, M., Berger, M., and Adomavicius, G., "A Parallel Multilevel Method for Adaptively Refined Cartesian Grids with Embedded Boundaries," *38th Aerospace Sciences Meeting*, 2000, AIAA Paper 2000-0808.

[2] Nemec, M. and Aftosmis, M., "Adjoint Error Estimation and Adaptive Refinement for Embedded-Boundary Cartesian Meshes," *18th AIAA Computational Fluid Dynamics Conference*, 2007, AIAA Paper 2007-4187.

[3] Aftosmis, M. and Rogers, S. E., "Effects of Jet-Interaction on Pitch Control of a Launch Abort Vehicle," *46th AIAA Aerospace Sciences Meeting and Exhibit*, 2008, AIAA Paper 2008-1281.

[4] Brauckmann, G. J., Greathouse, J. S., and White, M. E., "Rocket Plume Scaling for Orion Wind Tunnel Testing," *29th AIAA Applied Aerodynamics Conference*, 2011, AIAA Paper 2011-3341.

[5] Gusman, M. R., Barad, M. F., and Kiris, C. C., "Aerodynamic Database Generation for SRB Separation from a Heavy Lift Launch Vehicle," *29th AIAA Applied Aerodynamics Conference*, 2011, AIAA Paper 2011-3651.

[6] Pamadi, B. N., Pei, J., Gumbert, C. R., Green, L. L., Ross, J. M., Housman, J., Onufer, J., and Kiris, C., "Aerodynamic Modeling and Database Development of the Space Launch System Booster Separation," *53rd AIAA Aerospace Sciences Meeting*, 2015, AIAA Paper 2015-0779.

[7] Dalle, D. J. and Rogers, S. E., "Output-Based Adaptive Meshing Applied to Space Launch System Booster Separation Analysis," *33rd AIAA Applied Aerodynamics Conference*, 2015, AIAA Paper 2015-3152.

[8] Pamadi, B. N., Pei, J., Pinier, J. T., Holland, S. D., and Covell, P. F., "Aerodynamic Analyses and Database Development for Ares I Vehicle First-Stage Separation," *Journal of Aircraft*, Vol. 49, No. 5, 2012, pp. 864–874.

[9] Klopfer, G. H., Onufer, J. T., Pandya, S. A., Chan, W. M., Kless, J. E., and Lee, H. C., "Analyses of the Ares I A106-Plus Launch Vehicle First Stage Separation," Tech. Rep. FS-TR-00002, NASA, 2011.

[10] Nichols, R. H., Tramel, R. W., and Buning, P. G., "Solver and Turbulence Model Upgrades to OVERFLOW2 for Unsteady and High-Speed Applications," *36th AIAA Fluid Dynamics Conference*, 2006, AIAA Paper 2006-2824.

[11] Wilcox, F. J., Pinier, J. T., Chan, D. T., and Crosby, W. A., "Space Launch System Booster Separation Aerodynamic Testing in the NASA Langley Unitary Plan Wind Tunnel," *54th Aerospace Sciences Meeting*, 2016.

[12] Aftosmis, M. J. and Nemec, M., "Cart3D Simulations for the First AIAA Sonic Boom Prediction Workshop," *52nd Aerospace Sciences Meeting*, 2014, AIAA Paper 2014-0558.

[13] Buning, P. G. and Pulliam, T. H., "Cartesian Off-Body Grid Adaption for Viscous Time-Accurate Flow Simulations," *20th AIAA Computational Fluid Dynamics Conference*, 2011, AIAA Paper 2011-3693.

[14] Chan, D. T., Dalle, D. J., Pinier, J. T., Rogers, S. E., Wilcox, F. J., and Gomez, R. J., "Development and Uncertainty Quantification of the Space Launch System Near-Proximity Booster Separation Aerodynamic Database," *54th Aerospace Sciences Meeting*, 2016.

[15] Gusman, M. R., Housman, J., and Kiris, C., "Best Practices for CFD Simulations of Launch Vehicle Ascent with Plumes - OVERFLOW Perspective," *49th AIAA Aerospace Sciences Meeting*, 2011, AIAA Paper 2011-1054.